ConsenCUS

Experimental results to constrain the uncertainties of critical parameters or impact of processes

ConsenCUS-D4.3-Experimental results to constrain the uncertainties of critical parameters or impact of processes-v1-2304

Date	Version	Status	Initials	Changes Marked
28/03/2023	1		NA	
03/05/2023	2		NA	

The sole responsibility for the content of this publication lies with the authors. It does not necessarily represent the opinion of the European Union. Neither CINEA nor the European Commission are responsible for any use that may be made of the information contained therein.

This project has received funding from the European Union's Horizon 2020 research and Innovation programme under grant agreement N° 101022484.

Version Control Sheet

WP:	WP4 CO2 storage
Lead author:	Nikolai Andrianov
Contributing Authors:	Jing Ai, Jolanta Kazmierczak, Knud Dideriksen, Hanne Dahl Holmslykke, Hyojin Kim, Samira Mohammadkhani, Behzad Rostami, Rikke Weibel
Due date:	2023-04-30
Date:	2023-04-18
Version:	1
Contact:	nia@geus.dk

Dissemination Level:

■ PU: Public

☐ CO: Confidential, only for members of the consortium (including the Commission)

Executive summary 4
1 Materials and methods 5
1.1 Core samples 5
1.2 Formation brine 8
1.3 Core-flooding setup 9
1.4 Petrographical characterization 11
2 Core flooding experiment 12
2.1 Brine permeability measurement 12
2.2 Supercritical CO_2 flooding 13
2.3 Rock mechanical aspects of experiment 17
2.4 Salt precipitation and fines migration 18
3 Petrographical investigations 20
4 Geochemical modelling 24
4.1 Assumptions 24
4.2 Methods 25
4.3 Redox reactions in NO_X-SO_X-O_2 system 26
4.4 Kinetic reactions in gas-brine system 31
4.4.1 The rates of the chemical reactions 31
4.4.2 Kinetic reactions in diffusion dominated gas-brine system 35
4.4.3 Model set up 36
4.4.4 Reaction kinetics in diffusion dominated regime 37
5 Numerical modeling 44
5.1 Model setup 44
5.2 Simulation results 48
Conclusions 53
Bibliography 54

Executive summary

The results of the ConsenCUS WP4 deliverable D4.2 indicate that there are significant uncertainties in the parameters of rock-fluid interactions, which lead to considerable differences in estimating the CO_2 recovery efficiency during temporary storage. The goal of the present deliverable D4.3 is to reduce the uncertainties by conducting a core flooding laboratory experiment, accompanied by a petrophysical evaluation of rock alteration before and after the experiment, together with the corresponding geochemical and numerical modeling. The experiments were done using rock samples and at the reservoir conditions, characteristic for the potential CO_2 storage site at Stenlille.

The experimental results indicate that the rock mineralogy, samples permeability, and samples dimensions were essentially unaffected by CO_2 flooding. This means that there are only very limited geochemical and geomechanical effects are expected due to CO_2 interaction with the formation. On the other hand, sudden increases in differential pressure at the start of experiment have been observed, which can be possibly explained by pore blockage due to fines migration or salt precipitation. Precipitated salt and some fines were also detected after the end of experiment.

Numerical modeling is able to reproduce the experimental results reasonably well. The numerical results are most sensitive to the parameters of relative permeabilities and water vaporization into the CO_2 phase. In line with the experimental results, the predicted amount of precipitated salt is small, and the predicted sample's permeability does not change considerably. Overall, the results indicate the features of the numerical model which will be used on a reservoir scale to estimate storage efficiency at Stenlille and Havnsø sites (deliverable D4.4).

1 Materials and methods

1.1 Core samples

Three horizontal core plugs with numbers C11, C12, and C14 were plugged from Stenlille-6 well zone 3, whole core 3, box 12, from the interval 1584.38 to 1585.38 m measured depth (the well log is shown in Figure 5). Samples' photos are presented in Figure 1.

Figure 1. Images of the core plugs C11, C12 and C14 used in the experiment.

The samples' choice was made by analysing the X-ray computed tomography (CT) images in order to ensure samples' homogeneity. Figure 2 to Figure 4 demonstrate an overview of XY, XZ, and YZ orthogonal sections of the three samples with the same dimensional scaling and without cropping. All samples are imaged in plastic bottles. Note that the top and bottom of the images are affected cone beam imaging artifacts (seen as large diamond shapes).

The samples are relatively homogeneous with the following features:

- Sample C11: minor concentration of high-density features in several planes.

- Sample C12: minor concentration of high-density features in several planes in addition to apparent periodic fluctuations in the bulk density at the scale of 5-8 mm.
- Sample C14: less homogeneous distribution of high-density features in the sample in addition to minor concentration of high-density features in several planes.

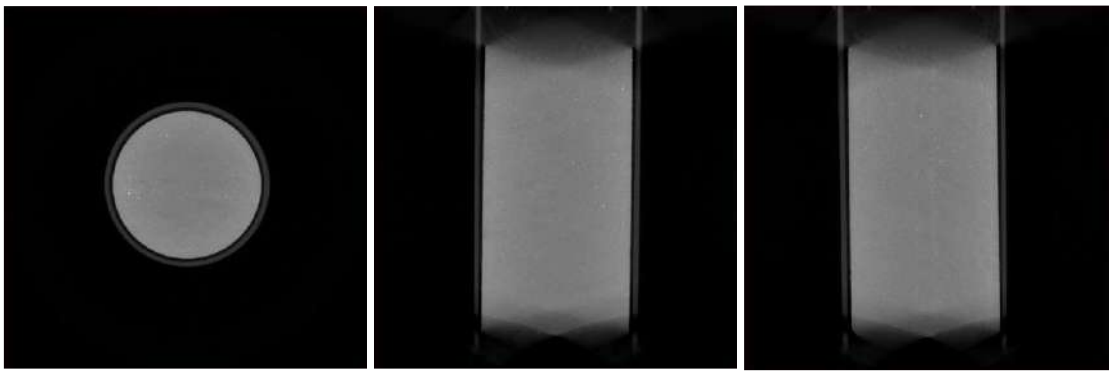

Figure 2. Sample C11: XY, XZ and YZ slices (left to right).

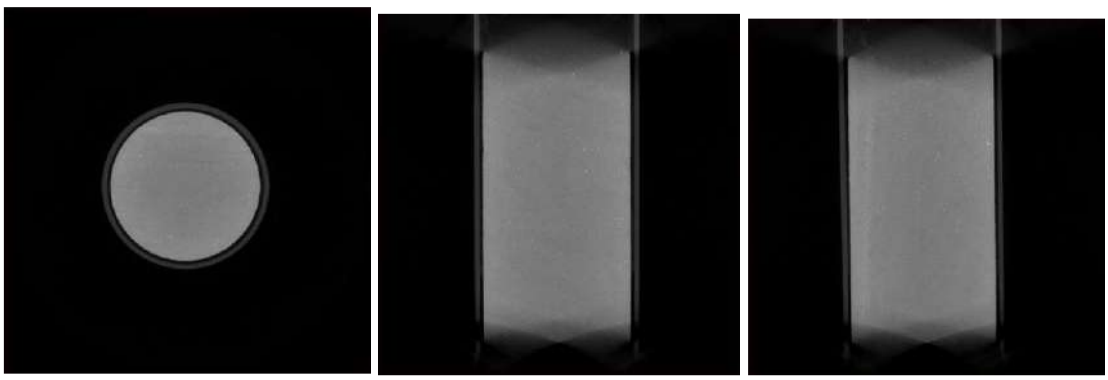

Figure 3. Sample C12: XY, XZ and YZ slices (left to right).

Figure 4. Sample C14: XY, XZ and YZ slices (left to right).

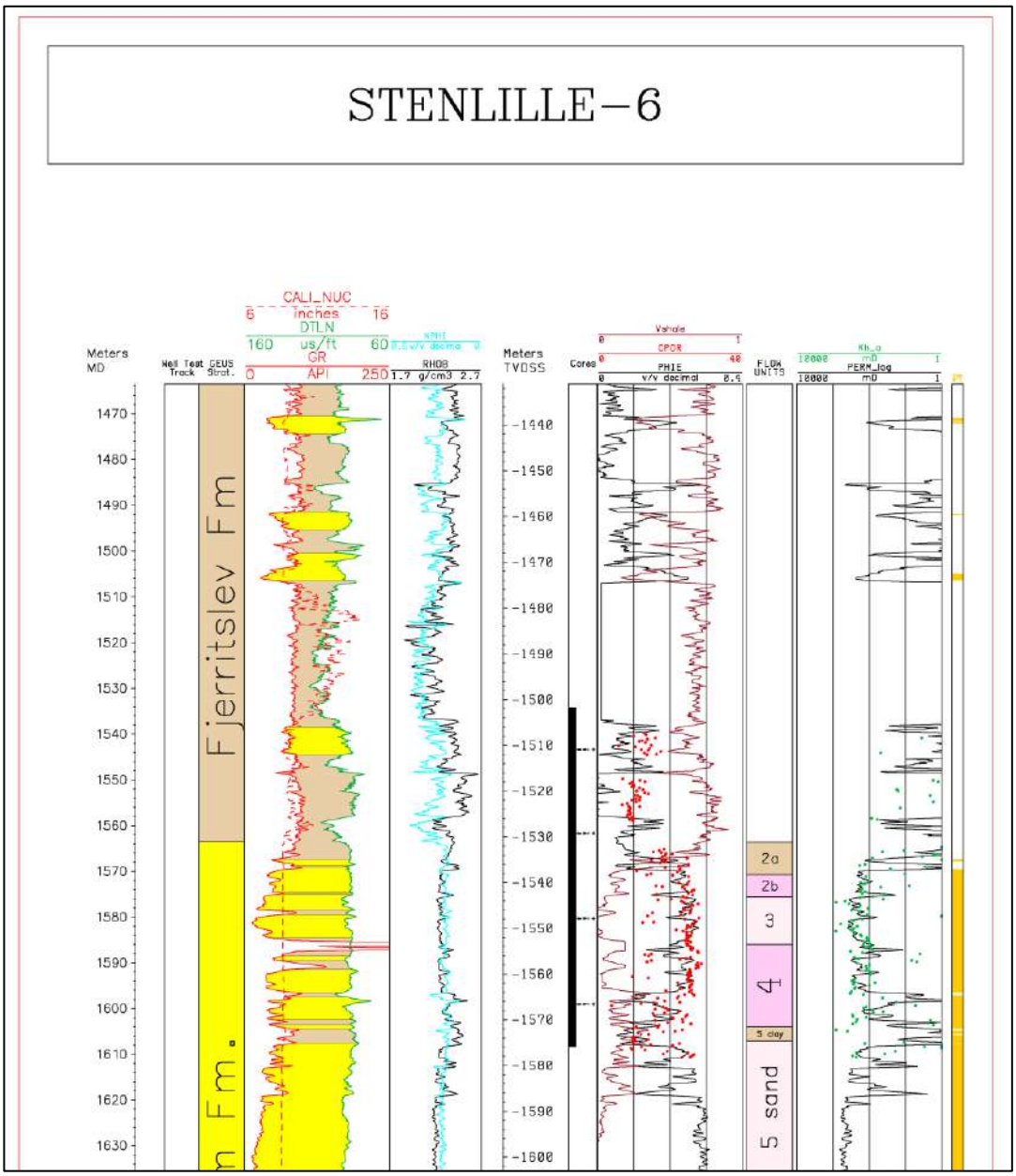

Figure 5. Stenlille-6 well log, the samples are plugged from box 12 core 3, in 1584.38 to 1585.38 m measured depth. The chosen rock material lays down in zone 3.

The core plugs were cleaned by flushing methanol through the core samples, mounted in separate core holders. The flow through cleaning was stopped when no chloride is detected in the effluents.

The samples' dimensions, porosity, permeability and grain density are presented in Table 1. The gas and Klinkenberg permeability were measured by nitrogen and porosity was calculated by measuring the bulk volume and grain density using mercury and helium. The samples were in a very fine consolidated state.

Table 1. Core plugs characteristics.

Sample ID	MD (m)	He poro (%)	N2 perm (mD)	Grain density (g/cm3)	Diam (cm)	Length (cm)	Hg bulk vol (ml)	Pore vol (ml)	Klink perm (mD)
C11	1584.95	24.8	131.3	2.65	3.80	7.38	82.50	20.43	119.41
C12	1584.99	25.1	139.0	2.66	3.79	7.49	83.70	20.97	127.00
C14	1585.07	24.8	132.1	2.66	3.79	7.47	83.33	20.66	120.90

1.2 Formation brine

The water used in the core flooding experiment is synthetic formation water with the composition similar to the produced water from Stenlille-1 well. The produced water has been tapped by Gas Storage Denmark from a free water separator without mixing, and the composition has been analyzed at GEUS. To avoid precipitation of insoluble minerals, the contents of HCO_3^- has been reduced; total iron concentration could not be measured as it was already precipitated in the sampling bottles. The produced water composition and the synthetic brine composition is presented in Table 2. Water was always degassed by evacuation before being used in the experiment.

Table 2. Synthetic brine, used to saturate core plugs, compared to the produced water from Stenlille.

Component or Parameter	Composition of produced water from Stenlille-1 well	Composition used in the experiment
Na^+ (mg/l)	59394	59394
Ca^{2+} (mg/l)	9964	9964
Mg^{2+} (mg/l)	1838	1838
K^+ (mg/l)	308	308
Br^-(mg/l)	422	422
Sr^{2+} (mg/l)	700.5	0

Cl^- (mg/l)	113146	114343
SO_4^{2-} (mg/l)	138	138
HCO_3^- (mg/l)	60	30
Salinity (wt%)	n.a.	16.6
TDS (mg/l)	n.a.	186032
Density (g/ml) @ 1 atm, 22 °C (1)	n.a.	1.123
Density (g/ml) @ 160.0 bara, 50 °C (2)	n.a.	1.117
Viscosity (cP) @ 160.0 bara, 50 °C (3)	n.a.	0.798

(1) Fluid density measured at GEUS with Paar DMA 35.
(2) Fluid density measured at GEUS with Paar DMA HPM.
(3) Brine viscosity at reservoir conditions calculated from (Kestin, et al., 1978).

1.3 Core-flooding setup

The three plugs (C11, C12, and C14) were saturated with synthetic brine and were mounted as a composite core sample in a hydrostatic core holder (Figure 6).

Figure 6. GEUS core flooding rig.

The core flooding experiment was run using 5-liter cylinders, a core holder, a two-phase separator, and a back pressure regulator. Core plugs and it´s appliances before mounting in the core holder are shown in Figure 7. Two steel sieves with 1 mm openings were placed at each end of the composite core sample. Two particle traps were installed inside the core holder to reduce the possibility of any blockage due to fine migration. These traps were aimed to catch the fines by the help of gravity. The conditions of the core flooding experiment are summarized in Table 3.

Figure 7. Three core plugs and the appliance for mounting the cores in the core holder.

Table 3. Conditions for the core flooding experiment.

Parameter	Value

Formation	Gassum Formation
Sample type	Composite of plugs C11, C12, and C14 from Stenlille-6 well
Temperature	50 °C
Fluid pressure	160 bar
Hydrostatic confining pressure	185 bar
Net overburden pressure	25 bar
Flow direction	Horizontal
Brine	Synthetic with the composition of Table 2
Injection **CO_2**	K.V. Gasteknik purity 4.0

1.4 Petrographical characterization

Petrographical characterization of the samples before and after experiments was performed by optical microscopy of polished thin sections besides scanning electron microscopy (SEM) of carbon-coated thin sections and platinum-coated rock chips. Zeiss Sigma VP field emission SEM equipped with two Bruker Xflash 6-30 30 mm2, 129 eV EDS detectors was applied, operating at 15 kV and 40–100 nA. Mineral abundances were quantified by point counting of minimum 500 minerals, exclusive porosity, in each thin section. In order to investigate salt precipitation during flooding with $scCO_2$, low vacuum mode was applied for SEM analysis of 'wet' samples taken immediately after de-pressuring of the core holder.

2 Core flooding experiment

The testing protocol for the core flooding experiment consisted of the following steps:

1. Mounting core holder with the composite sample of 3 core plugs from Stenlille-6 samples in GEUS FC Rig.
2. Setting up the reservoir condition of 160 bar and 50 °C.
3. Measurement of brine permeability @ 100 ml/h.
4. CO_2 flooding @ 200 ml/h, 6.6 PVs injected in 2.05 hours. A sudden increase in differential pressure was observed, which indicates pore blockage.
5. The CO_2 flow was reverted in order to avoid the pore blockage.
6. CO_2 flooding @ 200 ml/h, 142.4 PVs injected in 44.7 hours.
7. CO_2 flooding @ 1000 ml/h, 67.5 PVs injected in 4.1 hours.
8. CO_2 flooding @ 200 ml/h, 20.2 PVs injected in 6.35 hours.
9. Flooding stopped when the CO_2 container ran empty.
10. Depressurization and cooling of the reservoir rig.
11. Dismounting core holder from the rig & dismounting the plugs from the core holder.
12. Check both ends of the core holder for any signs of salt precipitation and/or fines.
13. Cleaning the samples and measuring the porosity, permeability, and analysis of eventual mineralogical alteration using scanning electron microscopy (SEM).

2.1 Brine permeability measurement

Permeability to brine was calculated from Darcy's law by using the constant flow rate of 100 ml/h and an estimate (Kestin, et al., 1978) of brine viscosity of 0.798 cP for the flow conditions of 50°C, 160 bara at salinity of 16.6 wt%, as illustrated in Figure 8. The resulting brine permeability is 110 mD. Note that this value if lower than the gas and Klinkenberg permeabilities of separate core plugs (Table 1), which is in line with the literature data (Bloomfield & Williams, 1995).

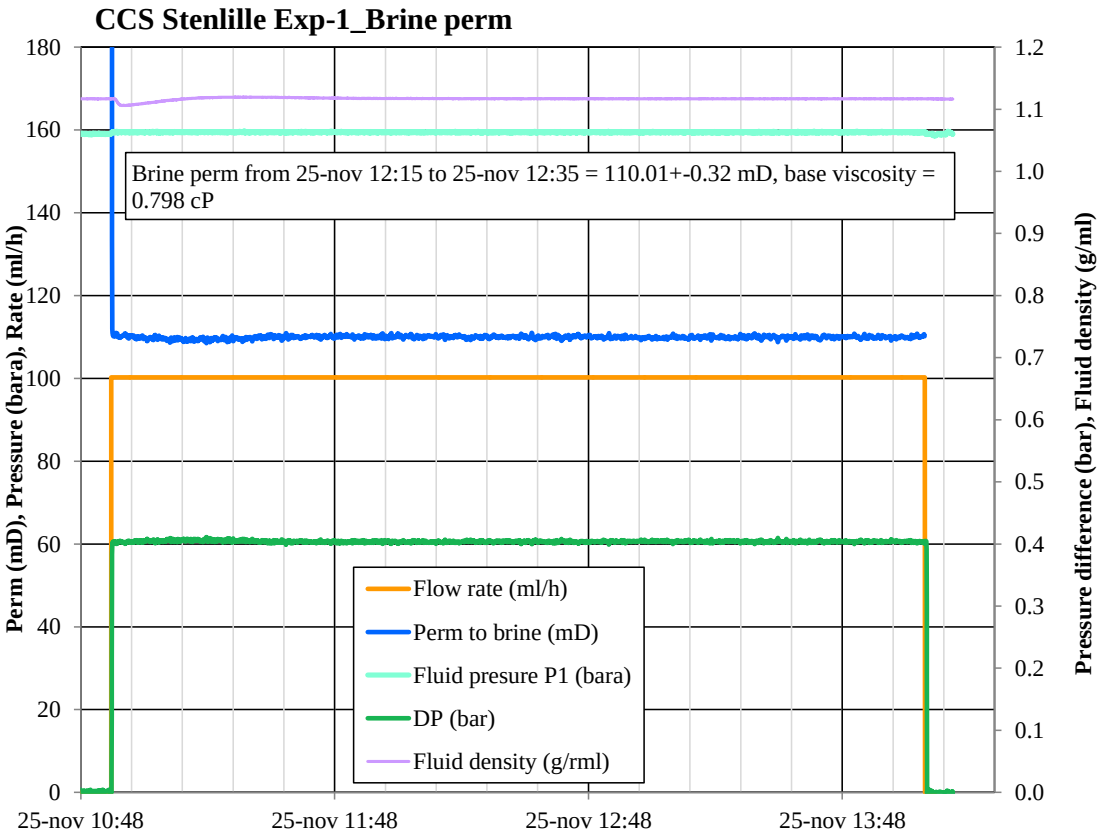

Figure 8. Estimating the brine permeability of the composite sample using steady-state core flooding results.

2.2 Supercritical CO_2 flooding

The injection of supercritical CO_2 ($scCO_2$) took place continuously for two and a half days when a total of 236 pore volumes (PVs) were injected in the brine-saturated composite core at constant injection rates of 200 ml/h and 1000 ml/h. Figure 9 presents the measured (differential pressure (dP), water saturation (Sw), effluent fluid density) and calculated (apparent permeability) data with regards to time, while Figure 10 presents the same data as a function of injected PVs. The pressure and temperature during the experiment were kept constant at 160 bara and 50 °C, respectively. The amount of produced water was monitored by an acoustic separator, which did not account for the CO_2 dissolution in brine.

A sharp 13-min increase in differential pressure occurred after 2-hours injection of 6.6 PVs of $scCO_2$, which indicated that the flow blockage has occurred, see a close-up in Figure 11. The flow direction of $scCO_2$ was reversed and the differential pressure curve returned to its trend before the blockage occurred. While the exact cause of this event is not known, it is speculated that it could have been caused by migration of small sand particles (fines) due to fluid drag, or by salt precipitation in the core.

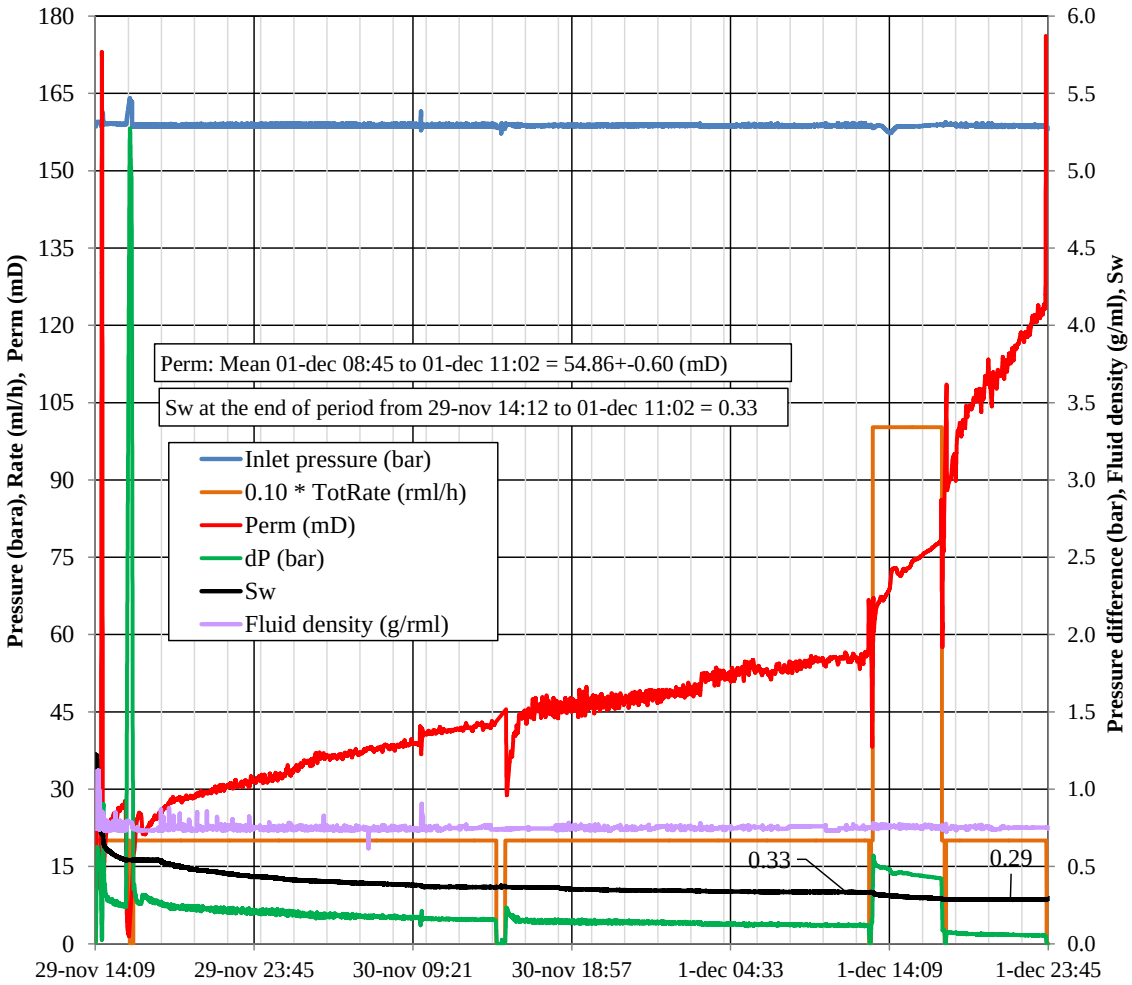

Figure 9. Core flooding results vs. time.

The flow is considered to be stable between 120 to 140 injected PVs, which yields the effective permeability to $scCO_2$ of 54.86 mD. At this point, the water saturation in the core is equal to 0.33. Note that the effective $scCO_2$ permeability is less than the initial brine permeability of 110 mD.

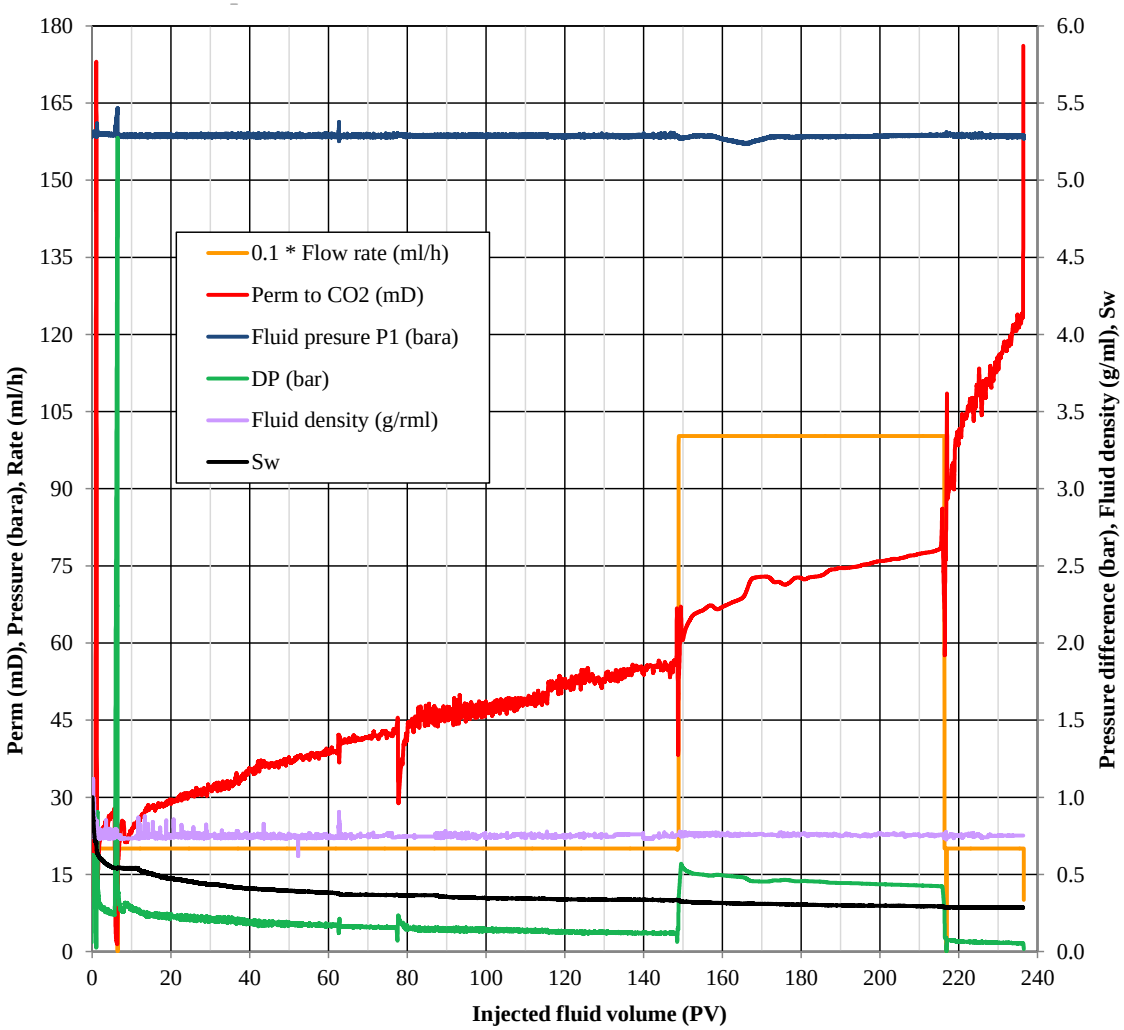

Figure 10. Core flooding results vs. injected PVs.

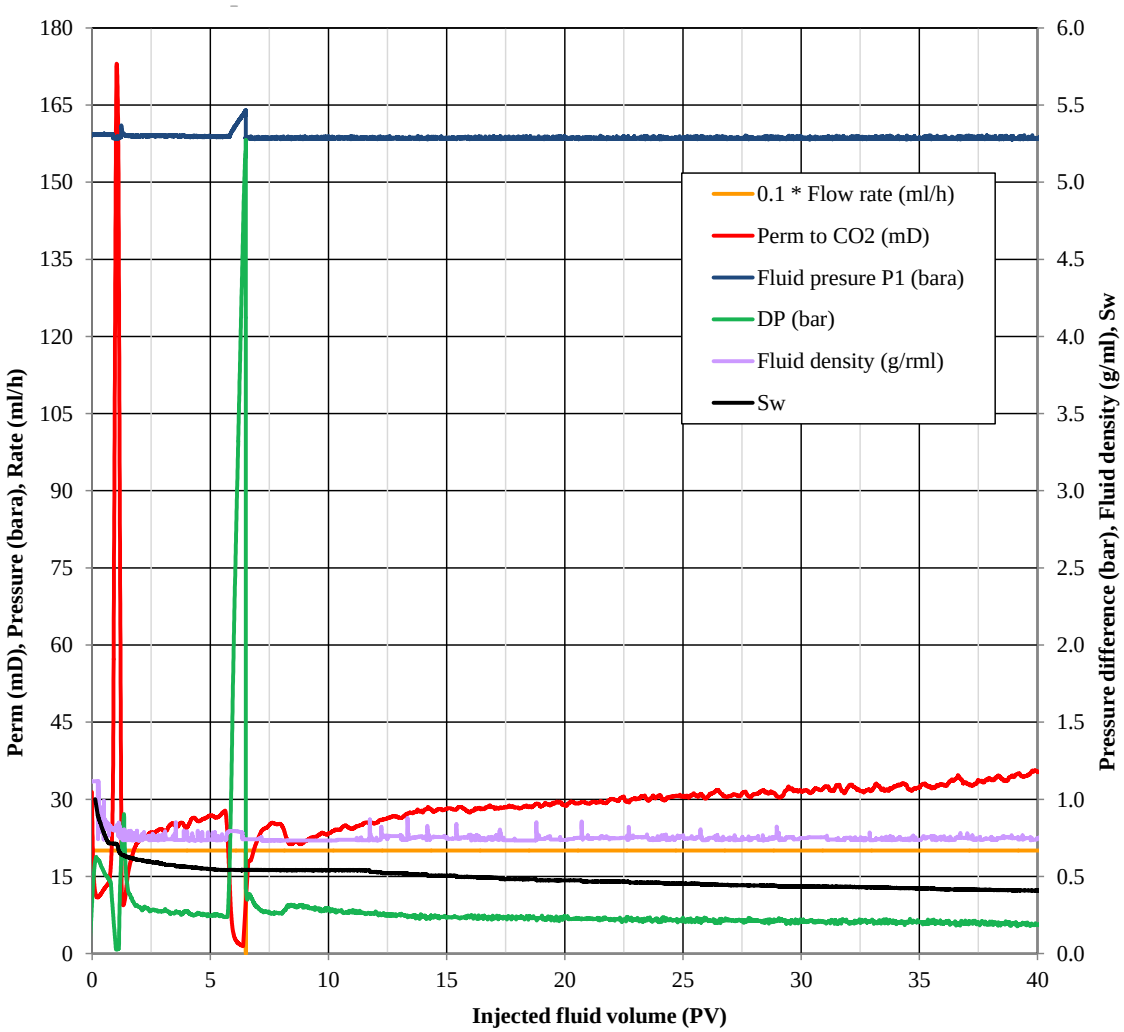

Figure 11. A zoom on the first hours of scCO_2 injection with a sharp increase in differential pressure, attributed to pore blockage.

The weight-measured water saturations at the end of experiment are presented in Table 4.

Table 4. Water saturations at the end of the core flooding experiment.

Sample ID	Final water saturation (%)
C11	14.39
C12	5.58
C14	10.99

2.3 Rock mechanical aspects of experiment

The length of composite core in the core holder is periodically measured using a floating piston, and the results are presented in Figure 12. The measurement accuracy is 0.04 mm. While there is a minor change in the length of sample due to interaction with CO_2, heating and pressurization/ depressurization, no damage has been detected in the samples after the experiment, cf. Figure 13.

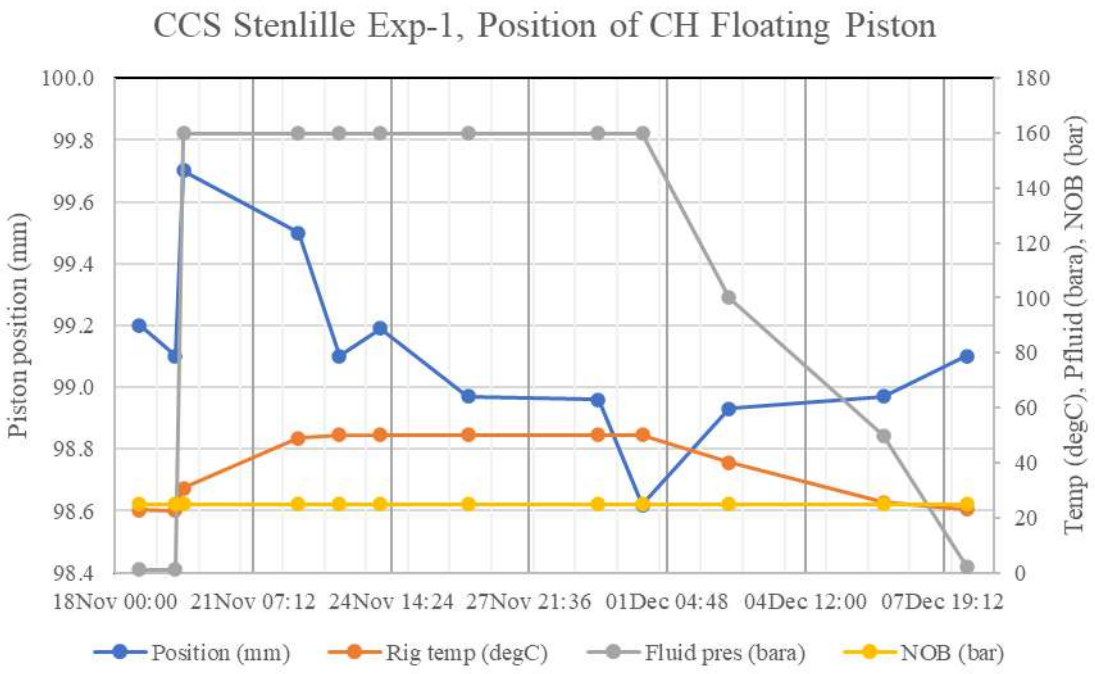

Figure 12. Dynamic change in the length of the composite sample during the core flooding experiment.

Figure 13. The core plugs after CO_2 flooding experiment. The inlet and outlet appear to be wet (higher content of water) and the core plug in the middle seems to be dry.

2.4 Salt precipitation and fines migration

After the end of the core flooding experiment, salt crystals and a small amount of fines were observed on the filter at the sample end, which corresponds to outlet for the initial flow direction (the flow direction was reverted after the flow blockage as described in Section 2.2); see Figure 14. The observed fines have possibly migrated during the initial $scCO_2$ injection before the flow blockage. However, the amount of fines is small so it is not clear whether they have caused the blockage. Also, there is no clear indication whether salt precipitation has occurred during or after the experiment.

Figure 14. the core samples outlet after opening the core holder after CO_2 flooding. The salt in the middle of the filter is shown in this picture. This outlet is the original outlet and further became inlet after changing the flow direction.

3 Petrographical investigations

The sandstones are fine-grained with rounded – subangular grains. The sandstones consist mainly of quartz, predominantly monocrystalline but also polycrystalline. Quartz grains occasionally have rounded overgrowths enclosing reddish coatings, which suggests recycling of a possible Triassic sediment. The feldspar group is composed of K-feldspar and rare amounts of plagioclase (Table 5). Feldspar grains commonly show various degrees of dissolution and occasionally clay mineral precipitation. Mica, mainly muscovite, is rare. Heavy minerals are rare and comprises rutile, tourmaline, zircon, leucoxene-replaced Fe-Ti oxides, titanite and possibly apatite.

Table 5. Modal composition of samples from Gassum Formation, before and after experiment.

Samples ID	**ST6-1584.95 (before exp.)**	**ST6-1584.95EX (after exp.)**
Quartz (mono+poly+chert)	84.7	83.2
K-feldspar	3.9	3.8
Plagioclase	0.6	0.6
Mica	0.2	0
Rock fragments and mud clasts	1.3	1.1
Heavy minerals	0.8	1.9
Quartz overgrowths	1	1.1
Feldspar overgrowths	0.2	0
Calcite cement	0.2	0.2
Pyrite	0	0.6
Anatase	0.3	0
Detrital clays	1.5	0.6
Drilling mud	5.5	6.6
Kaolin	0	0.2
TOTAL	**100**	**100**

The cementing phases, ordered with decreasing abundances, consist of quartz, calcite, kaolinite, pyrite, K-feldspar and anatase. Calcite occurs as rare patchy poikilotopic cement (Figure 15).

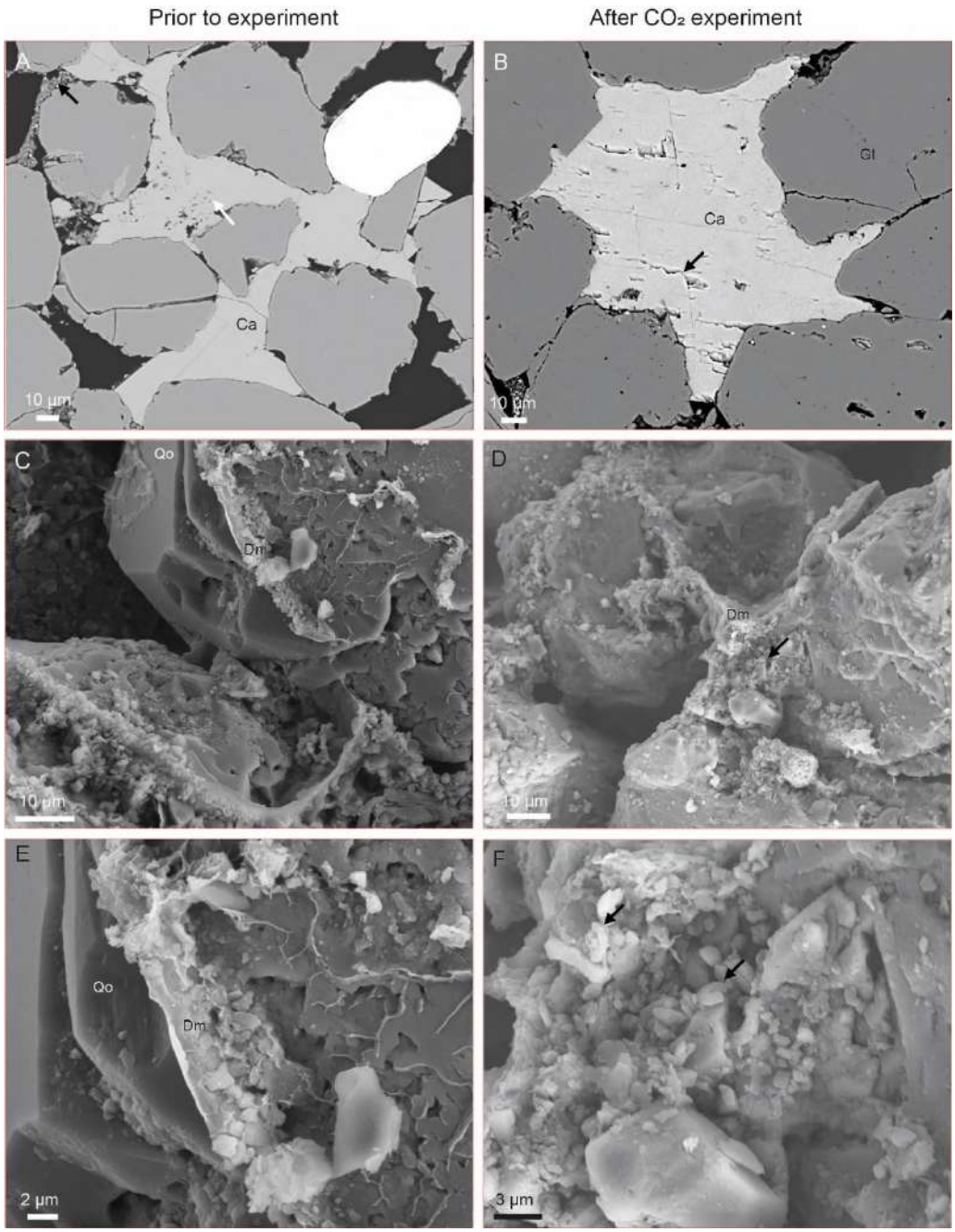

Figure 15. Mineralogical alterations during the flooding experiment. A. Calcite cement (Ca) with small inclusions kaolinite (white arrow). BSE micrograph. B. Calcite cement showing possible incipient dissolution features (arrow). BSE micrograph. C. Drilling mud (Dm), consisting of smectitic clays, calcite, quartz and kaolinite crystals, covering quartz overgrowth (Qo). SE micrograph. D. Drilling mud enclosing coccolith (arrow). SE micrograph. E. Close up of C. F. Close up of D.

Kaolinite occurs as rare pore-filling cement and occasionally inside altered feldspar grains. Pyrite framboids are occasionally enclosed in euhedral pyrite. Pyrite and anatase may occur next to altered Fe-Ti oxides. Quartz forms thin overgrowth on detrital quartz grains. K-feldspar commonly have optically discontinuous overgrowths.

The drilling mud consists of smectic clays with abundant tiny calcite fragments, besides quartz and kaolinite (Figure 15). Some of the calcite fragments can be identified as coccoliths (Figure 15D, Figure 15F). Drilling mud forms meniscus cement covering all authigenic phases, suggesting that it was infiltrated during drilling and settled after retrieving the cores.

After the experiment, no major changes were observed. The calcite cement seems remarkably little affected by the $scCO_2$ flooding, although microfractures seem to be more common in sandstones exposed to the experiment (compare Figure 15A with Figure 15B).

Most of the grains in the sandstones are unaffected by the $scCO_2$ flooding. Increased dissolution of feldspar grains cannot be confirmed since they showed dissolution features prior to the experiments. Calcite cement shows limited dissolution features (Figure 15A, Figure 15B). Previous batch experiments at reservoir conditions, where sandstones from the Gassum Formation was exposed to CO_2 dissolved in brine , showed carbonate cement dissolution (Weibel, et al., 2014). The low degree of calcite dissolution in the present sample is probably due to buffering by dissolution of tiny calcite fragments in the drilling mud.

The possibility of mobilising kaolinite could be a potential risk. However, fines migration is expected to have little influence on the reservoir quality in the Stenlille area due to a low abundance of kaolinite in the investigated samples (Table 5) and generally in the Gassum Formation from the Stenlille area (Weibel, et al., 2017).

Drilling mud is infiltrated into the sandstones in the core and presumably also in the Gassum Formation close to the well. The sandstones tested by lab experiments consequently mimic the near wellbore injectivity, which probably is improved away from the wellbore due to less infiltrated drilling mud.

Samples retrieved directly from the experiment showed the presence of salt covering all surfaces (Figure 16). The salt crystals consist of CaCl2, which is a hygroscopic mineral with a strong tendency to react with water vapor. Therefore, such salt precipitation is likely to be underestimated unless precautions are taken to investigate the samples immediately after

termination of the experiment. Calcite added to the drilling mud in the form of tiny crystals probably functioned as an easily dissolved Ca source, which in combination with the high Cl content in the formation water resulted in CaCl2 precipitation. Farther away from the borehole, dissolved calcite cement from the Gassum Formation may result in similar, though probably less, salt precipitation.

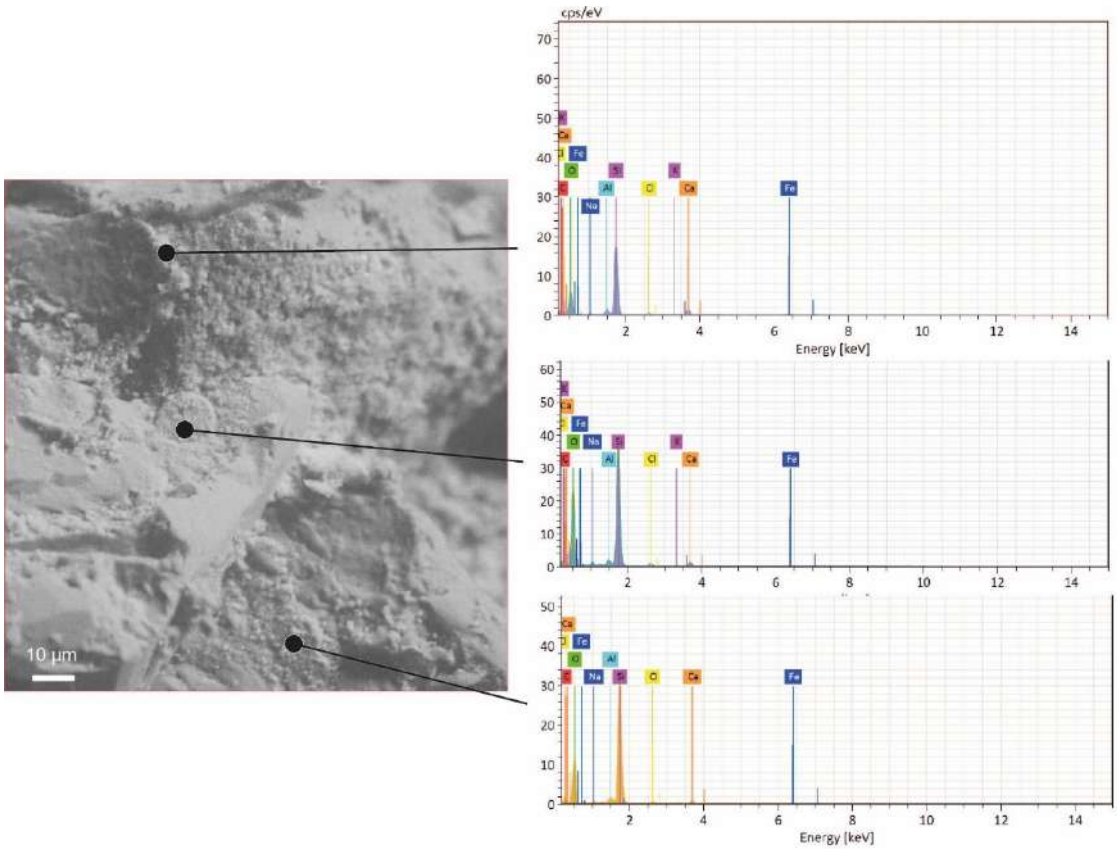

Figure 16. Salt precipitation (CaCl2) accompanying scCO_2 flooding. A. SE micrograph taken at low vacuum. B.C. and D. EDS analyses of salt crystals.

4 Geochemical modelling

4.1 Assumptions

The impact of near-well geochemical reactions is one of the key uncertainties for sustained injectivity of CO_2. The reactions and their impact depend on a range of parameters, such as the nature of the rock, the composition of the brine, and the injection strategy. The main component of captured gas stream is CO_2. However, the CO_2 will contain a variety of oxidizing and reducing impurities with concentrations depending on source, capture technique and processes downstream in the transport chain (Rütters, et al., 2022).

Several studies have been performed to assess the identity of the impurities and their likely maximum concentration (Talman, 2015), (Luna-Ortiz, Yao, Barnes, Winter, & Healey, 2022), (Rütters, et al., 2022). In addition, CCS projects in development have defined CO_2 specifications. Four examples of the maximum proposed impurity compositions are given in Table 5, listing only the constituents of likely importance for acidification. For the Northern Lights and Porthos projects, the compositions do not account for gas incompatibility, whereas (Rütters, et al., 2022) provide values for two types of compatible gasses. In what follows, we use the specifications given in (Luna-Ortiz, Yao, Barnes, Winter, & Healey, 2022) to form the basis for evaluation of geochemical reactions in the reservoir, focusing only on NO_2, SO_2, and O_2.

Table 6. Examples of the maximum concentrations of constituents of clear geochemical importance (mol based ppm) for injected CO_2.

Origin	Northern Lights	Porthos	Rütters et al., 2022		Luna-Ortiz et al., 2022 (PACE)
Type	-	-	Reducing	Oxidizing	-
O_2	10	40		6700	10
SO_x	10	20[1]		70	50[2]
NO_x	10	5		110	50[2]
H_2S	9	5[1]	50		5[3]
Ammonia	10	3			1500

[1] Subject to total sulphur compounds being less than 20 ppm.

[2] As NO2 and SO2 in our study of interaction with the reservoir rock.

[3] Total for H2S and COS.

When water is present, NO_2, SO_2, and O_2 interact through a series of fast redox reactions that take place in the near-well environment, e.g., (Spycher, Llanos, & Haese, 2019). The exact location where the reaction products accumulate would depend on many aspects such as injection rate, water distribution, dissolved ion reaction rates, mineral-water reaction rates, and mineral composition and surface area. Because of variable reaction rates for the different impurities, it is conceivable that different reaction products accumulate at different distance from the injection well. The redox reactions produce various acids, which will lower pH and promote rock dissolution. The rate at which the rock dissolves and the nature of the solid reaction products are unknown. If substantial dissolution occurs, it could jeopardize the structural integrity of the reservoir rock near the well. On the other hand, slow rock dissolution would not yield base for buffering of pH and could cause the waters close to the well to become highly acidic, potentially compromising infrastructure.

In what follows, we report on the development of a model that can be applied to study the influence of NO_2, SO_2, and O_2 in the CO_2 stream on brine composition and mineral dissolution. This information would allow use to conduct simulations of cyclic injection and obtain an estimate of the potential for formation damage or generation of a highly corrosive environment near critical infrastructure, both of which could challenge sustained injectivity and productivity.

4.2 Methods

Two-phase reactive transport simulation of the reactions occurring near the well upon injection/production of CO_2 with NO_2, SO_2 and O_2 requires that the pertinent reaction pathways are identified and the values for a substantial number of parameters are established. The parameters needed include those describing gas solubility of the impurities and their volatile reaction products (henceforth termed trace gasses when pooled), speciation and reaction rates of the dissolved trace gasses, their change in activity at the variable solution compositions, the dissolution rates of minerals and the identity of solid transformation products.

To establish these parameters our strategy has been to:

1. Determine the fastest of the reactions and establish the solubility of the trace gasses. Because of industrial and environmental importance, the reactions between NO_2, SO_2 and O_2 have been the subject of scientific studies for decades. Thus, much is known about the possible reactions and their rates. A review of this literature allowed us to determine likely impurity reaction pathways and reaction products that should be included in the model. For the gasses not already in the database, the Henry's constant was corrected for fugacity coefficients at reservoir temperature and pressure (60 °C and 200 bar). For the dissolved gasses, we implemented a rough model for activity coefficients as

a function of ionic strength. In addition, the speciation of new aqueous species was introduced into the thermodynamic database used in the simulations and the database was modified to allow for redox decoupling of aqueous species of Fe(II) and Fe(III).

2. Establish likely reaction kinetics for the reactions. From the review, it is clear that some of the reactions are so fast that the influence of mass transfer processes, such as diffusion, had to be accounted for in the experimental studies of the chemical reaction rates. Preliminary simulations indicated that for the faster of the reactions the concentration of the dissolved impurities in the water menisci of the sediment showed substantial simulated gradients because the chemical reactions were occurring at rates comparable to those of the diffusional mass transfer. In our simulation tool, all the water in a given cell is assumed to be in equilibrium with the gas present. This is clearly not likely to be the case for the faster reactions. Hence, these were subjected to a set of simulations to establish the net rates that would be a result of the reactions influenced by diffusion.
3. To enable reactive transport simulations of injection of impure CO_2 with ToughReact V4.13 and the ECO_2N module (Sonnenthal, Xu, Spycher, & Zheng, 2021), (Spycher, Zhang, Sonnenthal, & Molis, 2021) (Pruess, 2005), embed the new data for trace gas solubility in the Pitzer database tk-pitz1.ypf.R2.dat, including simplified description of the activity of the dissolved gasses as a function of solution composition.

Simulations of the impact of diffusion on net reaction rates were conducted with PHREEQC (Parkhurst & Appelo, 2013) using the Pitzer database (Plummer, Parkhurst, Fleming, & Dunkle, 1988).

4.3 Redox reactions in NO_X-SO_X-O_2 system

The oxidizing impurities comprising NO_2, SO_2 and O_2 undergo a range of reactions that involve the impurities themselves, their reaction products and water. The reactions can be catalyzed by dissolved metals and presumably by the presence of solid phases, similar to reaction between O_2 and Fe(II). Altered brine chemistry affects water-rock interactions and mineral dissolution and precipitation. A review of the major geochemical processes in the studied gas-brine-rock system is given below. The reactions either occur at equilibrium or are kinetically controlled. From the review of the literature, 16 reactions were selected because of their fast kinetics. These reactions produced several species that were not already in the tk-pitz1.ypf.R2.dat database. Thus, thermodynamic data for the species SO_2, NO_2, NO, N_2O, HNO_2, and HSO_3^- had to be defined.

Gaseous species (henceforth denoted with "(g)") dissolve in water and form aqueous species (denoted with "(aq)"):

$SO_2(g) \rightleftarrows SO_2(aq)$ Reaction 1
$NO(g) \rightleftarrows NO(aq)$ Reaction 2
$NO_2(g) \rightleftarrows NO_2(aq)$ Reaction 3
$N_2O(g) \rightleftarrows N_2O(aq)$ Reaction 4
$HNO_2(g) \rightleftarrows HNO_2(aq)$ Reaction 5

Gas dissolution is a fast, reversible process and is therefore considered as an equilibrium reaction. The equilibrium constants for reactions are defined with respect to activities (a_i) for aqueous species and fugacities (f_i) for gas species:

$$a_i = C_i \gamma_i. \quad \text{Equation 2}$$
$$f_i = P_i j_i. \quad \text{Equation 3}$$

Here, a_i refers to the activity of aqueous species *i*; C_i, to its concentration; and γ_i, to its activity coefficient. For the gas part, f_i refers to the fugacity of gas species *i*; P_i, to its partial pressure; and j_i, to its fugacity coefficient. Thus, Henry's constant (K_H), for gas *i* is defined as:

$$K_H = \frac{a_i}{f_i} = \frac{C_i \gamma_i}{P_i j_i}. \quad \text{Equation 4}$$

Equilibrium constants for gas dissolution with the uncharged aqueous species as reaction products are based on (Shock, Helgeson, & Sverjensky, 1989) for $SO_2(g)$, (Squadrito & Postlethwait, 2009) for $NO_2(g)$, and on the compilation by (Sander, 1999) for $NO(g)$, $N_2O(g)$, and $HNO_2(g)$. Henry's constants (K_H in mol atm^{-1} L^{-1}) reported for $SO_2(g)$ cover the temperature range 0–300 °C. The value of the constant at 60 °C was taken from (Shock, Helgeson, & Sverjensky, 1989) without changes. An equilibrium constant for $NO_2(g)$ dissolution at 20 °C (Squadrito & Postlethwait, 2009) was recalculated to be valid for 60 °C based on the given enthalpy of reaction and the Van't Hoff equation. For $NO(g)$, $N_2O(g)$, and $HNO_2(g)$ clearly outlying data in Sander (1999) were omitted and the equilibrium constants were recalculated to be valid for 60 °C based on the reported enthalpy of reaction and the Van't Hoff equation.

Formed $HNO_2(aq)$ deprotonates according to the reaction (Park & Lee, 1988):

$HNO_2(aq) \rightarrow NO_2^- + H^+$ Reaction 6

The equilibrium constant for deprotonation of HNO_2(aq) was taken from (Park & Lee, 1988) and recalculated to represent 60 °C based on the enthalpy of reaction. It was then combined with the equilibrium constant for HNO_2(g) dissolution (Reaction 5) taken from (Sander, 1999) to give the equilibrium constant for a net dissolution reaction of HNO2(g):

$$HNO_2(g) \rightarrow NO_2^- + H^+ \qquad \text{Reaction 7}$$

(Park & Lee, 1988) refrain from fitting of an activation energy because of the uncertainties this would entail. Thus, the equilibrium constants derived for Reactions 6 and 7 are likely quite uncertain.

Formed SO_2(aq) dissociates in the reaction (Shock, Helgeson, & Sverjensky, 1989):

$$SO_2(aq) + H_2O \rightarrow HSO_3^- + H^+ \qquad \text{Reaction 8}$$

Equilibrium Reactions 1–8 and their constants at 60 °C and 1 atmosphere pressure are summarized in Table 7.

Table 7. Impurities' reaction equations and equilibrium constants of the reactions at 60 °C (Log $K_{60\,°C}$).

Reaction	Log $K_{60\,°C}$
$SO_2(g) \rightleftarrows SO_2(aq)$	-0.2594
$NO(g) \rightleftarrows NO(aq)$	-2.9559
$NO_2(g) \rightleftarrows NO_2(aq)$	-2.2817
$N_2O(g) \rightleftarrows N_2O(aq)$	-2.0132
$HNO_2(g) \rightleftarrows HNO_2(aq)$	0.9526
$HNO_2(aq) \rightarrow NO_2^- + H^+$	-3.0062
$HNO_2(g) \rightarrow NO_2^- + H^+$	-2.0536
$SO_2(aq) + H_2O \rightarrow HSO_3^- + H^+$	-2.2563

Except for H_2O(g) and CO_2(g), the fugacity coefficient of gasses is assumed to be 1 in ToughReact V4.13 when combined with the ECO_2N module (Sonnenthal et al., 2021). Because fugacity coefficients may be quite different from unity, we updated the Henry's constants to reflect fugacity coefficients at the conditions of the reservoir. In this process, PHREEQC was employed

to establish the coefficients for the main trace gasses using the Peng-Robinson equation of state (Peng & Robinson, 1976) and values reported in the literature for critical temperature (T_c), critical pressure (P_{crit}) and acentric factor (ω). The calculations of fugacity with the Peng-Robinson equation of state in PHREEQC is given in (Appelo, Parkhurst, & Post, 2014) and (Parkhurst & Appelo, 2013). Briefly, the fugacity coefficient, φ, is calculated by:

$$ln\,\varphi = \left(\frac{PV_m}{RT_{(k)}} - 1\right) - ln\left(\frac{P(V_m - b)}{RT_{(k)}}\right) + \frac{a\alpha}{2.828\,b\,RT_{(k)}}\,ln\left(\frac{V_m + 2.414b}{V_m - 0.414b}\right), \quad \text{Equation 5}$$

Here, P represents pressure (atm); R, the gas constant (82.06 atm cm^3 mol^{-1} K^{-1}), V_m, the molar volume of the gas, b, the minimal volume of the gas, a, an attraction factor, a, a function of ω, temperature (in kelvin, $T_{(K)}$) and the critical temperature of the gas:

$$a = 0.457235\,\frac{(RT_c)^2}{P_{crit}}. \quad \text{Equation 5a}$$

$$b = 0.077796\,\frac{RT_c}{P_{crit}} \quad \text{Equation 5b}$$

$$\alpha = \left(1 + (0.37464 + 1.54226\omega - 0.26992\omega^2)\left(1 - \sqrt{\frac{T_{(k)}}{T_c}}\right)\right)^2. \quad \text{Equation 5c}$$

Provided, the pressure is given, V_m, can be determined:

$$P = \frac{RT}{V_m - b} - \frac{a\alpha}{V_m{}^2 + 2bV_m - b^2}, \quad \text{Equation 5d}$$

enabling the calculation of the fugacity coefficient (Appelo, Parkhurst, & Post, 2014).

For mixed gases, the weighted sums of a, b, and α are used in PHREEQC, assuming that binary interaction is negligible. With this assumption, PHREEQC calculations adequately describe the water fraction in CO_2 and the solubility of CO_2 in water from mixed CO_2-CH_4 gas (Appelo, Parkhurst, & Post, 2014).

Table 8 shows the values for critical temperature, critical pressure and acentric factor as well as the fugacity coefficient calculated with PHREEQC for 60 °C and 200 bar. Having established the coefficient (φ), the Henry's law constant was modified to yield a conditional constant valid for 60 °C and 200 bar (K_H*):

$$\log K_H^* = \log K_{H\,60°C} + \log \varphi. \quad \text{Equation 6}$$

The calculated log K_H* are given in Table 7 based on parameter values given in (American Petroleum Institute Data Book, 2005). Similar log K_H* were obtained with data from (Tosun, 2021) and (Camy, Letourneau, & Condoret, 2011).

In our ToughReact simulations, the activity coefficients are calculated with the Pitzer approach using the *tk-pitz1.ypf.R2.dat* database. However, we have had to introduce several new neutral species (the dissolved gasses) for which activity coefficients should be established. The real activity coefficient of the new species is likely to depend on solution composition in complex manner. Because this manner is unknown, we opted for a simpler description by introducing Pitzer parameters for the binary interaction between neutral species and all major ions so that the activity coefficient depended on ionic strength, I, defined as:

$$\mathrm{I} = 0.5 \sum_i C_i z_i^2. \qquad \text{Equation 7}$$

Here, Z_i refers to the charge of ion i. The values entered in the database were such that log g = 0.1 I, identical to the default equation for neutral species used in PHREEQC when more detailed information is lacking.

Clearly, this is likely to be a substantial simplification. However, to our knowledge Pitzer parameters do not exist for the dissolved gas species, we have introduced, and we note that the simplification at least allows for salting out of dissolved gasses at high ionic strength. Care should be taken when modifying Pitzer database because the interaction parameters for a pair of species (or triad) passes into the calculation of the activity coefficient of both species (or all three species of the triad). In these calculations, the impact of the interactions is weighed according to the concentration of the species. Given that the neutral species we have introduced occur only in minute quantities, they will not substantially affect the activity coefficients for the major ions. We have not introduced Pitzer parameters for the charged species, HSO_3^-, which means that its activity by default will be calculated using an extended Debye-Hückel type formulation.

The adequacy of the values we have introduced into the database were checked by conducting a series of simulations. PHREEQC was able to reasonably match (within 20%) the solubilities of pure NO and SO_2 at higher P given in (Rumpf & Maurer, 1992) and (Sterpenich, et al., 2022). Calculations of the solubility in water of 50 ppm of the trace gasses in CO_2 at 60 °C and 200 bar were identical for PHREEQC and ToughReact V4.13, and speciation diagrams for HNO_2 and SO_2 yielded the crossover between the concentration of protonated and less protonated species at the right pKa value.

Table 8. Conditional Henry's constants for the reactions at 60 °C at 200 bar (Log K_H) as well as the Tc, Pcrit and w used in the calculations (API data book, 2005), and the fugacity coefficient, φ, calculated with PHREEQC.*

Gas	T_c (K)	P_{crit} (atm)	*w*	***φ***	log $K_{H\ 60°C}$	log K_H*
NO	180.15	64	0.5846	2.32	-2.9559	-2.5898
NO_2	431.35	100	0.8486	0.10	-2.2817	-3.2767
N_2O	309.57	71.5	0.1418	0.41	-2.0132	-2.3999
SO_2	430.75	77.81	0.2451	0.11	-0.2594	-1.2111

4.4 Kinetic reactions in gas-brine system

4.4.1 The rates of the chemical reactions

The reactions between dissolved impurities and water are kinetically controlled and cannot be thoroughly described using the equilibrium concept. The major kinetic reactions identified in the NO_X-SO_X-O_2 system based on the literature review, their rates and power terms are summarized in Table 9.

SO_2(aq) is oxidized by O_2(aq) according to the reaction (Möller, 1988):

$$SO_2(aq) + H_2O + 0.5\ O_2(g) \rightarrow SO_4^{2-} + 2\ H^+ \qquad \text{Reaction 9}$$

The rate of SO_4^{2-} formation by Reaction 9 depends on pH, S(IV) species concentration and partial pressure of O_2(g). At pH between 4–12 and 25 °C it is described with a rate expression (Larson, Horike, & Harrison, 1977):

$$d[SO_4^{2-}]/dt = (k_{9a} + k_{9b}[H^+]^{0.5} + k_{9c}[pO_2(g)][H^+]^{-1})[S(IV)]$$

with $k_{9a} = 4.8 \times 10^{-3}$ mol^{-1} L s^{-1}, $k_{9b} = 8.9$ mol$^{-0.5}$ L$^{0.5}$ s^{-1}, and $k_{9c} = 3.9 \times 10^{-12}$ mol^{-1} L s^{-1}.

The reaction rate was adjusted to represent the system at 60 °C and dependence on O_2(aq) concentration. The corrected rate used in modelling is:

$$d[SO_4^{2-}]/dt = k_9[SO_2(aq)][O_2(aq)]$$

with $k_9 = 1.1 \times 10^{-2}$ mol^{-1} L s^{-1}.

Alternatively, $SO_2(aq)$ is oxidized by $NO_2(aq)$ and NO_2^- (Wang, et al., 2020):

$$SO_2(aq) + 2\ NO_2(aq) + H_2O \rightarrow SO_4^{2-} + 2\ H^+ + 2\ NO_2^- \quad \text{Reaction 10}$$

$$2\ SO_2(aq) + 2\ NO_2^- + H_2O \rightarrow 2\ SO_4^{2-} + 2\ H^+ + N_2O \quad \text{Reaction 11}$$

The rate of SO_4^{2-} formation by Reaction 10 depends on the concentration of S(IV) species, comprising $SO_2(aq)$ and HSO_3^- as well as the concentration of $NO_2(aq)$. For the pH range 5.3–6.8 the rate expression is given as:

$$d[SO_4^{2-}]/dt = k_{10}[NO_2(aq)][HSO_3^-]$$

with $k_{10} = 1.24 \times 10^7\ mol^{-1}\ L\ s^{-1}$ at pH near 5 (Clifton et al., 1988).

Kinetics of $SO_2(aq)$ oxidation by NO_2^- have been studied in the pH range 0.5–3.2 by (Martin, Damschen, & Judeikis, 1980) and for the pH range 1–5.5 by (Oblath, Markowitz, Novakov, & Chang, 1982).The rate of SO_4^{2-} formation by Reaction 11 derived by (Martin, Damschen, & Judeikis, 1980) depends on the total concentration of S(IV) species, comprising $SO_2(aq)$ and HSO_3^-, total concentration of N(III) species, comprising $HNO_2(aq)$ and NO_2^-, and pH:

$$d[SO_4^{2-}]/dt = k_{11}[H^+]^{0.5}[N(III)][S(IV)]$$

where $k_{11} = 142\ mol^{-3/2}\ L^{3/2}\ s^{-1}$ (Martin et al., 1980). The rate of SO_4^{2-} formation by Reaction 11 derived by (Oblath, Markowitz, Novakov, & Chang, 1982) depends on pH and HSO_3^- and NO_2^- concentrations:

$$d[SO_4^{2-}]/dt = k_{11}[H^+][NO_2^-][HSO_3^-]$$

where $k_{11} = 3800\ mol^{-2}\ L^2\ s^{-1}$ (Oblath, Markowitz, Novakov, & Chang, 1982). In our calculations, the rate derived by (Martin, Damschen, & Judeikis, 1980) is used.

$NO_2(aq)$ interacts also with water through disproportionation (Park & Lee, 1988):

$$2\ NO_2(aq) + H_2O \rightarrow NO_2^- + NO_3^- + 2\ H^+ \quad \text{Reaction 12}$$

The rate of $NO_2(aq)$ disproportionation depends on $NO_2(aq)$ concentration and is described by the rate expression:

$d[NO_2^-]/dt = k_{13}[NO_2(aq)]^2$

with $k_{12} = 8.4 \times 10^7$ mol^{-1} L s^{-1} (Park and Lee, 1988). For the NO_2(aq) disproportionation, (Park & Lee, 1988) provide reaction rates that decrease slightly with increasing temperature (10–30 °C). Here, we have used the value for 22 °C, which (Park & Lee, 1988) report as the most accurate.

NO_2^- reacts with H^+ to form HNO_2(aq) that disproportionates into NO(aq) and NO_2(aq) following the reaction (Park & Lee, 1988):

$$2\ HNO_2(aq) \rightarrow NO(aq) + NO_2(aq) + H_2O \qquad \text{Reaction 13}$$

(Park & Lee, 1988) provide rate constants for the forward and reverse direction of Reaction 13. The forward reaction rate depends on HNO_2(aq) concentration and is described by the rate expression:

$d[NO(aq)]/dt = k_{13}[HNO_2(aq)]^2$

To derive the rate at 60 °C, the values given for experiments at 10–30 °C in (Park & Lee, 1988), were fitted to the Arrhenius equation to establish activation energy and the pre-exponential factor, allowing extrapolation of reaction rates to 60 °C. The determined rate constant, k_{13}, at 60 °C is 4.36×10^2 mol^{-1} L s^{-1}.

The reverse reaction was implemented through ToughReact's option to allow the forward reaction rate (r_f) to be modified by the degree of disequilibrium to yield the net rate (r_{net}):

$$r_{net} = r_f \left(1 - \frac{Q}{K}\right). \qquad \text{Equation 8}$$

Here, K refers to the equilibrium constant and Q to the product of the actual activities expressed similarly to K. For Reaction 13:

$$Q = \frac{a_{NO(aq)} a_{NO_2(aq)} a_{H_2O(aq)}}{a_{HNO_2(aq)}{}^2}, \qquad \text{Equation 9}$$

where a_i refers to actual activities. The nature of Equation 8 is such that values of Q larger than 1 will provide for negative net reaction rates, i.e., the reverse rate. To establish the equilibrium constant from the reported rates, it was assumed to take the value $K = k_f/k_b$, where K_f refers to the forward rate constant and k_b, the rate constant for the reverse reaction. The rate constant for the reverse reaction given in (Park & Lee, 1988) shows little temperature dependence. Hence, we used the average value determined, 1.74×10^8 mol^{-1} L s^{-1}, yielding log K = -5.60. Because the

kinetic reaction had to be expressed with the primary species, NO_2^-, the equilibrium constant had to be recast to include the HNO_2 deprotonation (Reaction 6), leading to an equilibrium constant, log K, of 0.41. Note that (Park & Lee, 1988) did not fit an activation energy because of uncertainties. Thus, the values we have derived are most likely somewhat inaccurate.

Produced NO(aq) reacts with HSO_3^- following the reaction (Littlejohn, Hu, & Chang, 1986):

$$2\ NO(aq) + HSO_3^- \rightarrow SO_4^{2-} + H^+ + N_2O \qquad \text{Reaction 14}$$

The reaction rate at 25 °C and pH near 4 is:

$$d[SO_4^{2-}]/dt = k_{14}[NO(aq)][HSO_3^-]$$

where $k_{14} = 32\ mol^{-1}\ L\ s^{-1}$ (Littlejohn, Hu, & Chang, 1986).

Alternatively, NO(aq) is oxidized by $O_2(aq)$ following the reaction (Ignarro, Fukuto, Griscavage, Rogers, & Byrns, 1993), (Lewis & Deen, 1994):

$$4\ NO(aq) + O_2(aq) + 2\ H_2O \rightarrow 4\ NO_2^- + 4\ H^+ \qquad \text{Reaction 15}$$

The reaction rate derived at 37 °C and at pH 4.9 and 7.4 is:

$$d[NO_2^-]/dt = 4 \times k_{15}[NO(g)]^2[O_2(g)]$$

where $k_{15} = 2.4 \times 10^6\ mol^{-2}\ L^2\ s^{-1}$ and is pH independent (Lewis & Deen, 1994).

Finally, aqueous Fe^{2+} is oxidized by $O_2(aq)$ (Millero, Sotolongo, & Izaguirre, 1987):

$$Fe^{2+} + H^+ + 0.25\ O_2(aq) \rightarrow Fe^{3+} + 0.5\ H_2O \qquad \text{Reaction 16}$$

The homogenous oxidation rate given by (Millero, Sotolongo, & Izaguirre, 1987) depends on pH, salinity and temperature. For the conditions of the reservoir, we estimate that rate expressed as:

$$d[Fe^{3+}]/dt = k_{16}[Fe^{2+}][O_2(aq)]$$

where $k_{16} = 2.4 \times 10^{-5}\ mol^{-1}\ L\ s^{-1}$.

The rate constant was calculated assuming that the pH dependence is constant at lower pH (~4.5 occurring during CO_2 injection), based on findings reported at lower temperature (e.g. (Morgan, Lahav, & O., 2007)).

Table 9. Reaction rates and power terms for interactions between oxidizing mixture of impurities and water.

Reaction	Rate [mol^{-1} L s^{-1}]	Power terms		
$SO_2(aq) + H_2O + 0.5\ O_2(aq) \rightarrow SO_4^{2-} + 2\ H^+$	1.1×10^{-2}	$[SO_2(aq)]$	$[O_2(aq)]$	
$SO_2(aq) + 2\ NO_2(aq) + H_2O \rightarrow SO_4^{2-} + 2\ H^+ + 2\ NO_2^-$	1.24×10^7	$[NO_2(aq)]$	$[HSO_3^-]$	
$2\ SO_2(aq) + 2\ NO_2^- + H_2O \rightarrow 2\ SO_4^{2-} + 2\ H^+ + N_2O$	142	$[H^+]^{0.5}$	[N(III)]	[S(IV)]
$2\ NO_2(aq) + H_2O \rightarrow NO_2^- + NO_3^- + 2\ H^+$	8.4×10^7	$[NO_2(aq)]^2$		
$2\ HNO_2(aq) \rightarrow NO(aq) + NO_2(aq) + H_2O$	4.49×10^8	$[HNO_2(aq)]^2$		
$2\ NO(aq) + HSO_3^- \rightarrow SO_4^{2-} + H^+ + N_2O$	32	$[NO(aq)]$	$[HSO_3^-]$	
$4\ NO(aq) + O_2(aq) + 2\ H_2O \rightarrow 4\ NO_2^- + 4\ H^+$	2.4×10^6	$[NO(aq)]^2$	$[O_2(aq)]$	
$Fe^{2+} + H^+ + 0.25\ O_2(aq) \rightarrow Fe^{3+} + 0.5\ H_2O$	2.4×10^{-5}	$[Fe^{2+}]$	$[O_2(aq)]$	

4.4.2 Kinetic reactions in diffusion dominated gas-brine system

Gas-liquid reactions occur in three regimes that can limit their rates: 1) phase-mixed, where observed rates reflect the chemical reaction, 2) convective mass-transport limited, where observed rates are convoluted by the process of fluid mixing, and 3) diffusive mass-transport limited, where observed rates are convoluted by diffusional mass transfer rates. In addition, intermediate regimes exist (Danckwerts, 1970); (Lee & Schwartz, 1981). The mass transfer processes may have substantial impact on net rates of reaction. For example, (Lee & Schwartz, 1981) found in the laboratory experiments that the kinetic rate for Reaction 12 at fixed *P* NO_2 varies by a couple orders of magnitude, depending on the limiting reaction regime of their system. Furthermore, the dominating transport regime for Reaction 12 changes with changing *P* NO_2 (Lee & Schwartz, 1981).

Kinetic rates for Reactions 9–16 were derived for experimental conditions with gaseous and aqueous NO_X, SO_X, and O_2 species homogeneously distributed in the well mixed liquid column. Thus, the kinetic reaction rates summarized in Section 5.4.1 were obtained in the convective

mass-transport limited regime, and the actual rates of the chemical reactions were interpreted using theoretical considerations to correct for the effect of mass transfer. At a CO_2 injection site, there is little mechanical mixing of the gas stream with brine, and CO_2 with impurities is originally present at the edge of the water film surrounding mineral grains. Gas-brine interactions are therefore assumed to be diffusion limited. Thus, they will likely occur at lower rates than the rates for the chemical reactions (e.g., (Martin, Damschen, & Judeikis, 1980); (Park & Lee, 1988)). To avoid overestimation of the reaction kinetics, rates for Reactions 9–16 were corrected to account for diffusion using numerical modelling.

4.4.3 Model set up

For a hypothetical reaction, $X \rightarrow Y$, with the chemical reaction rate $d[Y]/dt = k\,[X]^n$, k and n would take different values if the equation is to describe the net reaction rate in the film including the influence of diffusion (e.g., (Lee & Schwartz, 1981)). The aim of the simulations reported here was to theoretically calculate the change in average concentration in the film of reaction products as a function of the concentration of the reactant at the gas-water interface. For our hypothetical reaction, we would thus simulate the concentrational change of Y in the film, $d[Y]_{film}/dt$, as a function of [X] at the gas-water interface, $[X]_{IF}$. This data set would then allow us to optimise the values of k and n, so that the rate equation now describes net rates in the water film. For this approach to be strictly valid, the simulated $d[Y]_{film}/dt$ should be related to the concentration of $[X]_{IF}$ by the equation $\log (d[Y]_{film}/dt) = \log k + n\,[X]_{IF}$. Hence, we will depict the outcome of the simulation and the fitting in logarithmic space.

The simulations were based on the assumption that diffusion from the gas-water interface into the water meniscus is Fickian so that the flux (J) would be the product of the diffusion coefficient in water (D) and the concentration gradient ($\frac{dC}{dx}$):

$$\mathrm{J} = -\mathrm{D}\,\frac{dC}{dx} \quad , \qquad \text{Equation 10}$$

In our simulations we assumed that the diffusion coefficients of the trace gasses were identical to that determined for CO_2, $4 * 10^{-9}$ $m^2\,s^{-1}$ at 60°C and 200 bar (Cadogan, Maitland, & Martin Trusler, 2014). The simulations were conducted for the Reactions 9–13, that were found to be of the highest importance in the considered system. Kinetics of Reaction 15 are slow at the concentrations of the gas stream and it is unlikely that the reaction is constrained by diffusion. PHREEQC models were set up in two steps. First, the accuracy of the software in prediction of products of the kinetic reactions was tested in a 1D model consisting of two 1.5×10^{-7} m long cells. In the next step, the kinetic reactions in the diffusive mass-transport limited regime were modelled in 1D column representing water meniscus of thickness 6×10^{-6} m (Figure 17). Model

sensitivity to discretization was assessed by increasing the number of cells in the 1D model column until the results of two subsequent simulations were comparable. The final model was subdivided into 40 cells of 1.5×10^{-7} m.

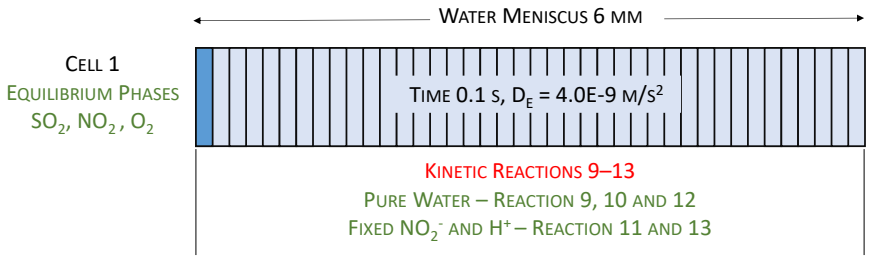

Figure 17. Generalized set up of the model for simulation of Reactions 9–13 in the diffusive mass-transport limited regime.

Solution in the first cell was equilibrated with the reactants, NO_2, SO_2 and O_2 at log *P* ranging from -3.8 to -0.8 for NO_2 and SO_2, and from -4.5 to -1.5 for O_2. The remaining cells in the models set up for Reactions 9, 10 and 12 contained pure H_2O. In the simulations of Reactions 11 and 13 solutions in all cells had pH fixed at 3 or 4.4 and were equilibrated with NO_2^- at log NO_2^- ranging from -3 to -0.5. Kinetic reactions 9–13 were assigned to the entire 1D column and simulated reaction time was 0.1 s, which was sufficient for generation of profiles that were invariant with time (i.e., a steady state had been reached). Each reaction was represented by an ensemble of 8–96 models with varying concentration of reactants. Production rate for each combination of reactants was estimated based on the reaction rates listed in Section 4.2.1. The estimated product concentrations in the film were fitted to the simulated product concentrations in the diffusive mass-transport limited regime by adjusting reaction rate and power terms until reaching the lowest sum of squared residuals between simulated values and those calculated with the rate equation using optimised values for the constant and exponents (henceforth called fitted).

4.4.4 Reaction kinetics in diffusion dominated regime

The accuracy check showed that the PHREEQC simulations using Pitzer database correctly predict the reaction rates when the product concentrations are up to 10 mol kgw^{-1}. At the product concentrations greater than 10 mol kgw^{-1} the model predictions significantly deviate from the analytical solutions. The best fit between the simulation results and analytical solution is acquired at the product concentration up to approximately 2.5 mol kgw^{-1} (Figure 18). Concentration of products of Reaction 9–13 in 1D column representing the water meniscus do not exceed 1 mol

kgw^{-1}. Thus, the simulation results are accurate and can be used for estimation of the reaction rates in the diffusive mass-transport dominated regime.

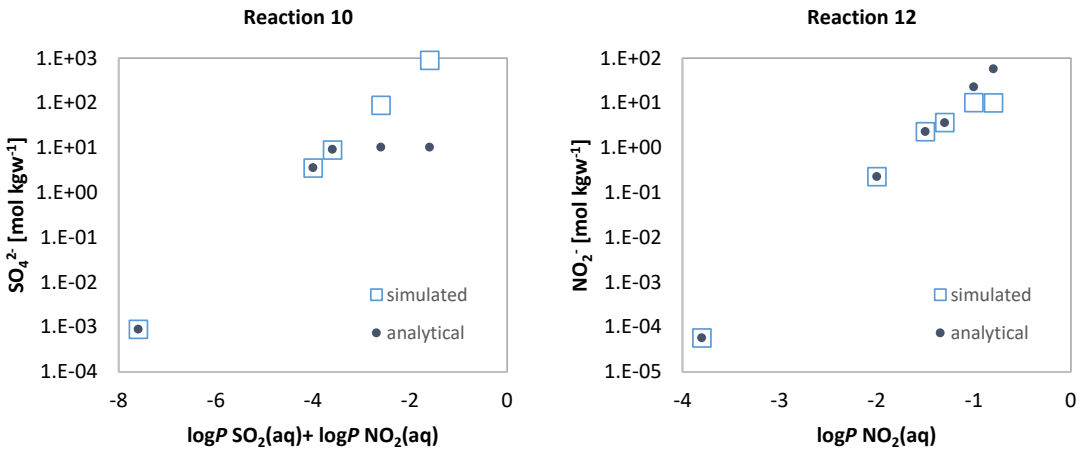

Figure 18. Simulated vs. analytical solution of the reaction rate for SO_2(aq) oxidation by NO_2(aq), Reaction 10, and NO_2(aq) disproportionation (Reaction 12).

The rate of SO_4^{2-} formation from SO_2(aq) oxidation by O_2(aq) is low and thus not significantly influenced in the diffusive mass-transport limited regime. The reaction rate estimated from simulation of Reaction 9 in the diffusion limited system decreases only by 0.05 compared to the reaction rate derived from the laboratory experiments and is expressed as:

$$d[SO_4^{2-}]/dt = k_9[SO_2(aq)][O_2(aq)]$$

with $k_9 = 1.05 \times 10^{-2}$ mol^{-1} L s^{-1}. SO_4^{2-} production at varying reactant concentrations in the diffusive mass-transport limited regime is shown in Figure 19. In this plot, the values should fall on a plane if the rate equation can adequately describe the simulated concentration. This is clearly the case. The maximum SO_4^{2-} concentration after 0.1 s is reached at log *P* SO_2(aq) of -0.8 and log *P* O_2(aq) of -1.5 and equals 3.7×10^{-9} mol kgw^{-1}. To compare, oxidation of SO_2(aq) at log *P* of -0.8 by NO_2(aq) at log *P* of or NO_2^- fixed at -0.5 yields 0.1 and 0.03 mol SO_4^{2-} kgw^{-1}. Similar to Reaction 9, the rate of Reaction 16 is slow at the conditions, at the order of 10^{-5} mol^{-1} L s^{-1} and would not be significantly influenced by diffusion. Thus, the simulations for Reaction 16 in the diffusive mass-transport limited regime were omitted.

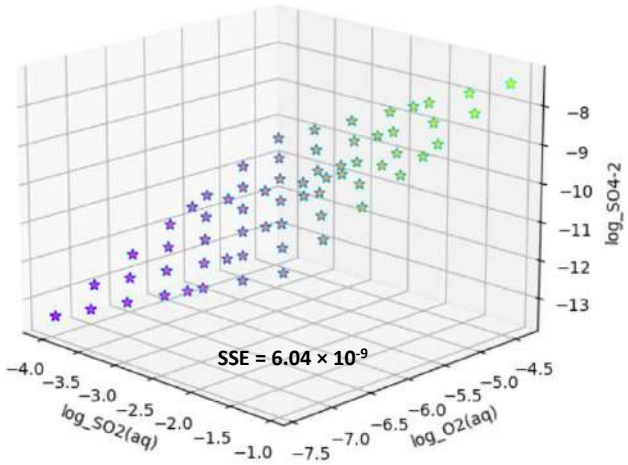

Figure 19. Simulated (dots) vs. fitted (stars) SO_4^{2-} production rate at varying SO_2(aq) and O_2(aq) concentrations.

The rate constant of Reaction 10 in the diffusive mass-transport limited regime decreases with increasing reactant concentration, as indicated by the simulations ensemble (Figure 20). A notable rate decrease occurs when the sum of logarithms of SO_2(aq) and NO_2(aq) concentration is ≥ -6. Thus, the simulated product concentrations were divided into two groups, where the sum of logarithms of SO_2(aq) and NO_2(aq) concentration was: (1) < -6, and (2) ≥ -6. The fitting of the rate equation was done for each group separately (Figure 21).

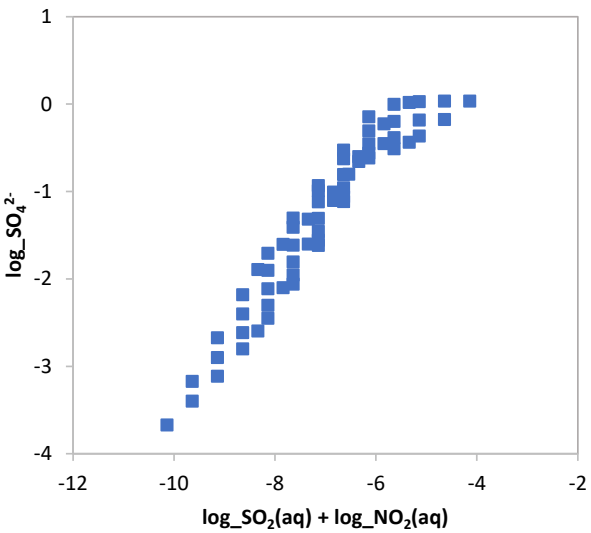

Figure 20. Changes in rate of SO_4^{2-} formation from SO^2(aq) oxidation by NO_2(aq) with varying reactant concentrations.

The rate of SO_4^{2-} formation from SO_2(aq) oxidation by NO_2(aq) in the diffusion limited regime at log[SO_2(aq)] + log[NO_2(aq)] less than -6 is:

$$d[SO_4^{2-}]/dt = k_{10}[NO_2(aq)][S(IV)]^{0.67}$$

where k_{10} = 1.06 × 10^5 mol^{-1} L s^{-1} and S(IV) is a sum of SO_2(aq) and HSO_3^- concentration. At log[SO_2(aq)] + log[NO_2(aq)] greater than or equal -6 the Reaction 10 rate decreases to:

$$d[SO_4^{2-}]/dt = k_{10}[NO_2(aq)]^{0.39}[S(IV)]^{0.03}$$

with k_{10} = 19.3 mol^{-1} L s^{-1}. It is notable that with increasing reactant concentrations the dependence of the reaction rate on the total concentration of S(IV) species is significantly decreased.

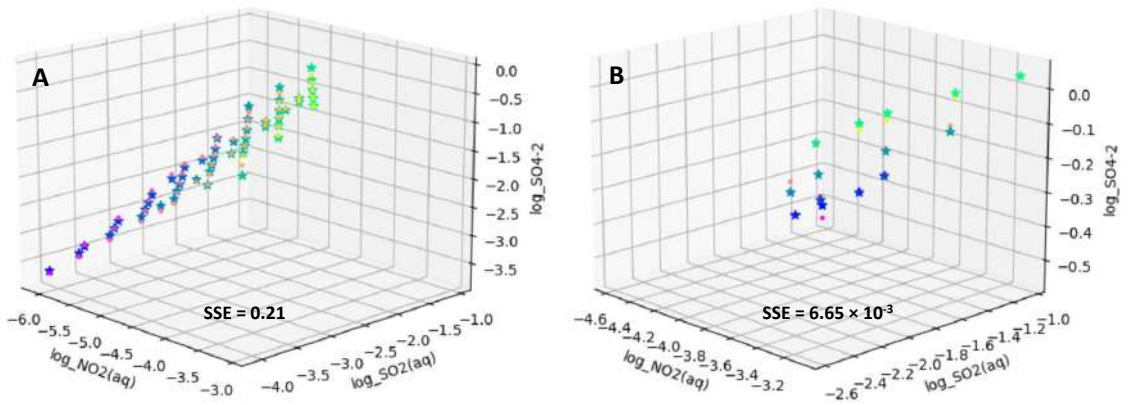

Figure 21. Simulated (stars) vs. fitted (dots) SO_4^{2-} production rate at varying SO_2(aq) and NO_2(aq) concentrations at (A) log[SO_2(aq)] + log[NO_2(aq)] < -6, and (B) log[SO_2(aq)] + log[NO_2(aq)] ≥ -6.

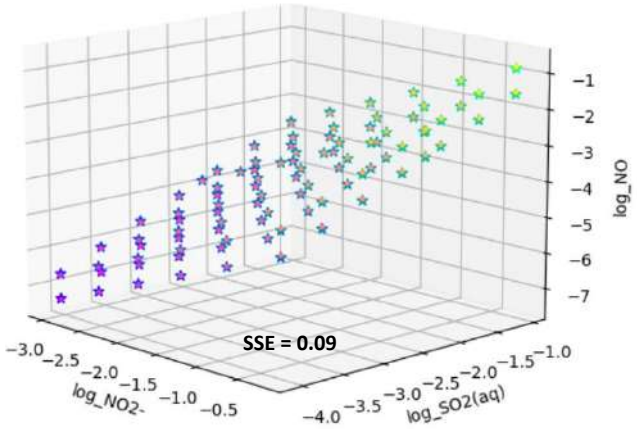

Figure 22. Simulated (dots) vs. fitted (stars) NO production rate at varying SO_2(aq) and NO_2^- concentrations.

The rate of S(IV) species oxidation by N(III) species comprising NO_2^- and HNO_2(aq) is low and reduced by less than half in the diffusive mass-transport limited regime:

$$d[SO_4^{2-}]/dt = k_{11}[H^+]^{0.5}[N(III)][S(IV)]$$

where k_{11} = 76.85 $mol^{-3/2}\ L^{3/2}\ s^{-1}$ (Figure 22). Similarly, even lower rate of Reaction 14, HSO_3^- oxidation by NO(aq), would not be significantly influenced by diffusion. Thus, the Reaction 14 rate in the diffusive mass-transport limited regime was not estimated and remained unchanged.

The rate of nitrous acid decomposition by Reaction 12 in the diffusive mass-transport limited regime decreases to:

$$d[NO_2^-]/dt = k_{12}[NO_2(aq)]^{1.5}$$

with $k_{12} = 5.74 \times 10^4\ mol^{-1}\ L\ s^{-1}$ (Figure 23).

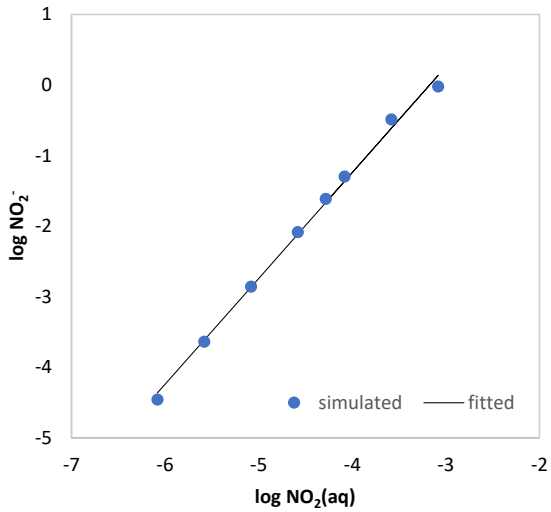

Figure 23. Rate of nitrous acid decomposition in the diffusive mass-transport limited regime.

Reaction 13 in the diffusive mass-transport limited regime was modelled using the modified reaction rate:

$$d[NO(aq)]/dt = k_{13}[NO_2^-]^2[H^+]^2(1-Q/K\_eq)$$

where $k_{13} = 4.49 \times 10^8$ mol^{-1} L s^{-1}, K_eq is an arbitrary equilibrium constant that equals $10^{0.41}$, and Q is the activity product:

$$Q = [NO][NO_2(aq)]/ [NO_2^-]^2[H^+]^2$$

The reaction quickly approaches equilibrium in the tested range of NO_2^- concentrations (log NO_2^- varied between -0.8 to -3.8) and at pH 3 and 4.4 (Figure 24, Table 10). Thus, the reaction rate is not significantly reduced in the diffusive mass-transport limited regime, and the original reaction rate was applied in the further modelling. Similarly, the rate of Reaction 15 is fast, and the reaction would not be significantly limited by the diffusion. Thus, the simulations for Reaction 15 in the diffusive mass-transport limited regime were omitted.

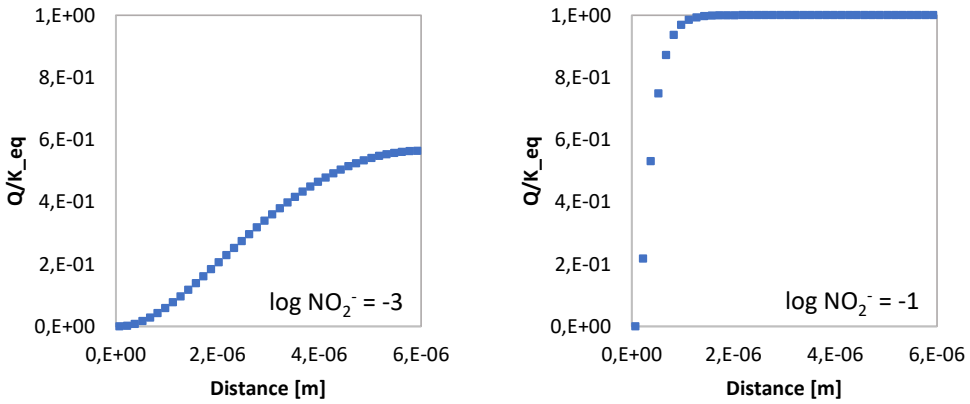

Figure 24. Equilibrium of Reaction 13 in the diffusive mass-transport limited regime at pH 3 and after 0.1 s of simulation.

Table 10. Equilibrium of Reaction 13 in the diffusive mass-transport limited regime after 0.1 s at varying pH and NO_2^- concentration.

pH	log [NO_2^-]	Q/K_eq
3	-0.5	0.74
	-1.0	0.94
	-1.5	0.93
	-2.0	0.92
	-2.5	0.92
	-3.0	0.92
4.4	-0.5	0.93
	-1.0	0.92
	-1.5	0.92
	-2.0	0.92
	-2.5	0.92
	-3.0	0.92

5 Numerical modeling

The results of Sections 2 and 3 indicate that there are only very limited geochemical effects due to CO_2 flooding and these are not affecting the samples permeability. Also, the samples' dimensions remain unchanged after CO_2 injection, which indicates that the potential geomechanical effects are negligible. On the other hand, precipitated salt is visible in SEM image, and salt crystals and some fines have been observed at the core outlet after the end of experiment. Also, there are sudden increases in differential pressure at the start of experiment, which can be possibly explained by pore blockage due to fines migration or by salt precipitation.

In what follows, we numerically model several of the above effects in order to get more insight into the fluids-rock interaction due to CO_2 injection in Stenlille rocks. The simulations below are conducted using the commercial simulator GEM (CMG, 2022), which allows for modelling of a wide range of thermodynamic and geochemical effects during CO_2 storage.

5.1 Model setup

The composite sample of Section 1.1 is considered as one-dimensional homogeneous porous medium 22.34 cm long with an average diameter of 3.79 cm, average porosity of 0.2487 and permeability of 134.05 mD. The simulations are done at isothermal conditions of 50 °C.

The composite sample is assigned a mineralogical composition, presented in Table 11. The considered minerals include quartz, K-feldspar, and calcite, which are the most ubiquitous minerals in the petrographical characterization (Table 5). In addition, halite, calcium chloride, and magnesium sulphate are included to model a potential precipitation.

Table 11. Mineralogical composition for numerical model.

Mineral name	Initial volume fraction	Molar mass (g/mol)	Density (kg/m3)
Quartz (SiO_2)	0.847	60.0843	2648.29
Feldspar ($KAlSi_3O_8$)	0.039	278.332	2556.55
Calcite ($CaCO_3$)	0.002	100.089	2709.95

Halite (NaCl)	0	58.4428	2163.35
Calcium chloride hydrate ($CaCl_2 \cdot xH_2O$)	0	129.001	2150
Magnesium sulphate ($MgSO_4$)	0	120.363	2659.95

The brine properties, used in the simulations below, are presented in Table 12. The initial compositions are calculated from the corresponding values of the synthetic brine, used in in the core flooding experiment (Table 2). The ion sizes and the charge numbers are the default values from the simulator GEM (CMG, 2022), used to calculate the components' activities in the B-dot model (Helgeson, 1969).

Table 12. Synthetic brine, used to saturate core plugs, compared to the produced water from Stenlille.

Component name	Initial molality (mol/kgw)	MW (g/mol)	Ion size (Å)	Charge number
H+	1.00E-07	1.0079	9	1
Ca++	0.25	40.08	6	2
Mg++	0.0757615	24.305	8	2
K+	0.0079	39.0983	3	1
Na+	2.74653	2.30E+01	4	1
SO4--	0.00143684	9.61E+01	4	-2
Al+++	1.00E-10	26.9815	9	3
SiO2	1.00E-10	6.01E+01	-0.5	0
Cl-	3.64159	3.55E+01	3	-1
HCO3-	1.00E-10	6.10E+01	4.5	-1
OH-	1.00E-10	17.0073	3.5	-1
CO3--	1.00E-10	60.0092	4.5	-2

Since CO_2 and water are mutually soluble, the fluid system contains two liquid phases, which are referred to as the CO_2-rich and water-rich (or aqueous) phases. The phase transitions between these phases are modelled with Peng-Robinson equation of state (Peng & Robinson, 1976), using the parameters, specified in Table 13. Methane is introduced as a tracer component.

Table 13. Parameters for the Peng-Robinson equation of state for the modelled fluid system.

	CO_2	CH4	H2O
Molar mass (g/mol)	44.01	16.04	18.01
Acentric factor	0.225	8e-3	0.344
Critical pressure (atm)	72.8	45.4	217.6
Critical volume (m3/k-mol)	9.4e-2	9.9e-2	0.056
Critical temperature (°K)	3.04e2	1.9e2	647.3
Parachor	78	77	52
Specific gravity	0.818	0.3	1
Average normal boiling point (°C)	-1.092e2	-2.58e2	100
Omega-A	0.457	0.457	0.457
Omega-B	0.077	0.077	0.077
Volume shift	0	0	0

Water vaporization into the CO_2-rich phase is allowed for water saturations above 0.1 only.

Table 14 lists the the default values for the binary interaction parameters from the simulator GEM (CMG, 2022), which are used In the simulations below.

Table 14. Binary interaction parameters for the considered fluid components.

	CO_2	CH_4	H_2O
CO_2	0		
CH_4	0.103	0	
H_2O	0.2	0.49	0

The viscosity of the CO_2-rich phase is calculated using the correlations (Herning & Zipperer, 1936), (Yoon & Thodos, 1970), (Jossi, Stiel, & Thodos, 1962).

Henry's law is used to calculate the solubilities of CO_2 in the aqueous phase with the reference Henry's constant of 9.06e4 kPa at the reference pressure of 3.55e3 KPa, and the partial molar volume at infinite dilution of 3.6e-2 l/mol. Methane's solubility in water is ignored.

The activity coefficients of aqueous species are calculated with the B-dot model (Helgeson, 1969).

The aqueous phase viscosity is calculated using the correlation (Kestin, et al., 1978).

During the simulations, porosity can change dynamically due to solid deposition, mineral precipitation or dissolution, or due to aqueous phase adsorption. The corresponding change in permeability K between the time steps n and $n+1$ is accounted by the relationship

$$K^{n+1} = K^n / r_f,$$

where the resistance factor r_f is calculated as a function of porosity ϕ with the Kozeny-Carman type formula

$$r_f = \left(\frac{\phi_n}{\phi_{n+1}}\right)^{r_e}$$

with the exponent $r_e = 3$.

The relative permeabilities are taken in the Brooks–Corey form (Brooks & Corey, 1964):

$$k_{rw} = K_w \left(\frac{S_w - S_{wc}}{1 - S_{wc} - S_{nc}}\right)^{n_w} \qquad k_{ro} = K_n \left(\frac{1 - S_w - S_{nc}}{1 - S_{wc} - S_{nc}}\right)^{n_n},$$

where S denote the saturations, the subscripts w, n refer to the wetting (water) and non-wetting (CO_2-rich) phases, respectively, S_{pc} is the critical phase saturations, n_p is the Brooks–Corey exponent, and K_p is the endpoint permeability for the phase $p = w, n$.

The chemical reactions, considered in the simulations below, are presented in Table 15. The reactions 1–3 are the aqueous phase chemical equilibrium reactions, which are characterized by the corresponding equilibrium constants K_{eq}. The reactions 4–6 are mineral precipitation or dissolution reactions, which are considered to be fast so that they can be modelled as equilibrium reactions. Finally, the reactions 7–9 are mineral precipitation or dissolution reactions, which are modelled as kinetic reactions. In addition to the equilibrium constants K_{eq}, the values of the initial reactive surface area A_0, the activation energy E_a, and the rate constant k_0 at the reference temperature t^* are provided in Table 15. The values of the parameters from Table 15 are the defaults from the simulator GEM (CMG, 2022).

Table 15. The chemical reactions, used for numerical modeling of the core flooding experiment.

No	Reaction	$\log K_{eq}$ at 50°C	A_0 (m2/m3)	E_a (J/mol)	$\log k_0$	t^* (°C)
1	$H_2O + CO_2 \rightleftarrows HCO_3^- + H^+$	-6.32				
2	$H_2O \rightleftarrows H^+ + OH^-$	13.26				
3	$HCO_3^- \rightleftarrows H^+ + CO_3^-$	10.23				
4	$KAlSi_3O_8 + 4H^+ \rightleftarrows 3SiO_2 + Al^{3+} + K^+ + 2H_2O$	-0.34				
5	MgSO4(c) ⇄ SO4-- + Mg++	3.73				
6	$CaCl_2.H2O \rightleftarrows 2Cl^- + Ca^{2+} + H_2O$	7.46				
7	$NaCl \rightleftarrows Cl^- + Na^+$	1.63	2163.35	7400	-0.21	25
8	$CaCO_3 + H^+ \rightleftarrows HCO3^- + Ca^{2+}$	1.36	2709.95	23500	-5.81	25
9	$SiO_2 \rightleftarrows SiO_2(aq)$	-3.63	2650	90900	-13.4	25

5.2 Simulation results

Given the considerable uncertainty in the relative permeabilities for Stenlille rocks, we consider the six Brooks-Corey parameters

$$S_{wc}, S_{nc}, n_w, n_n, K_w, K_n$$

as tunable parameters to match the experimentally measured differential pressure and water saturation (cf. Figure 9 and Figure 10).

Fitting the experimental results was done manually; the Brooks-Corey parameters which yield the best fit are presented in Table 16.

Table 16. The Brooks-Corey parameters which yield the best fit to the core flooding results.

S_{wc}	S_{nc}	n_w	n_n	K_w	K_n
0.35	0.1	4	2	1	0.33

The plots for the history-matched relative permeabilities are presented in Figure 25.

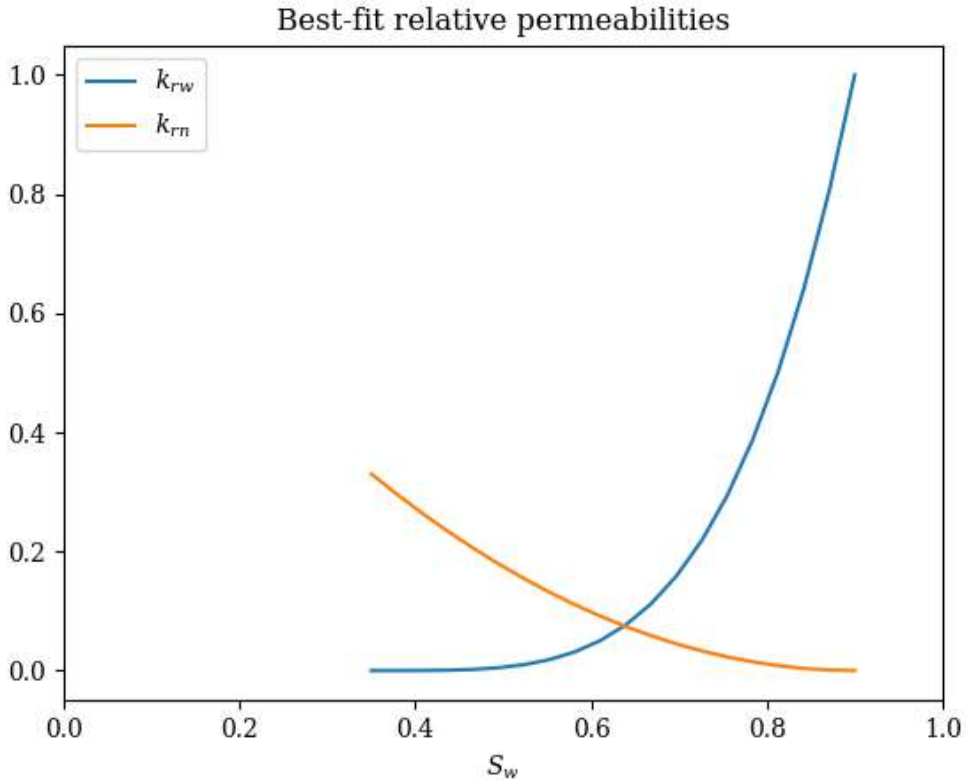

Figure 25. The relative permeabilities, manually fitted to match the experimental core flooding results.

A comparison of the experimental and numerical results is presented in Figure 26. For approximately 2 hours from the start of the experiment, a reasonably good match is achieved for both differential pressure and the saturation.

There are two peaks in the experimental data for the differential pressure at the start of the experiment at approx. 1 hour and 2 hours after the start of the experiment. The first event occurs after injection of approx. 1 PV of CO_2 in the core (cf. Figure 11) and the flow continues. The second event is characterized by a much larger differential pressure jump of approx. 5 bar (cf. Figure 11) after which the flow direction is reverted (see Section 2.2).

Reverting the flow in the numerical simulation causes a sharp drop in differential pressure at approx. 2.15 hours after the start of the experiment. After that, a good match is observed until approx. 20 hours. After that, the numerical results for the differential pressure match well the experimental values, but the results for saturation start to deviate.

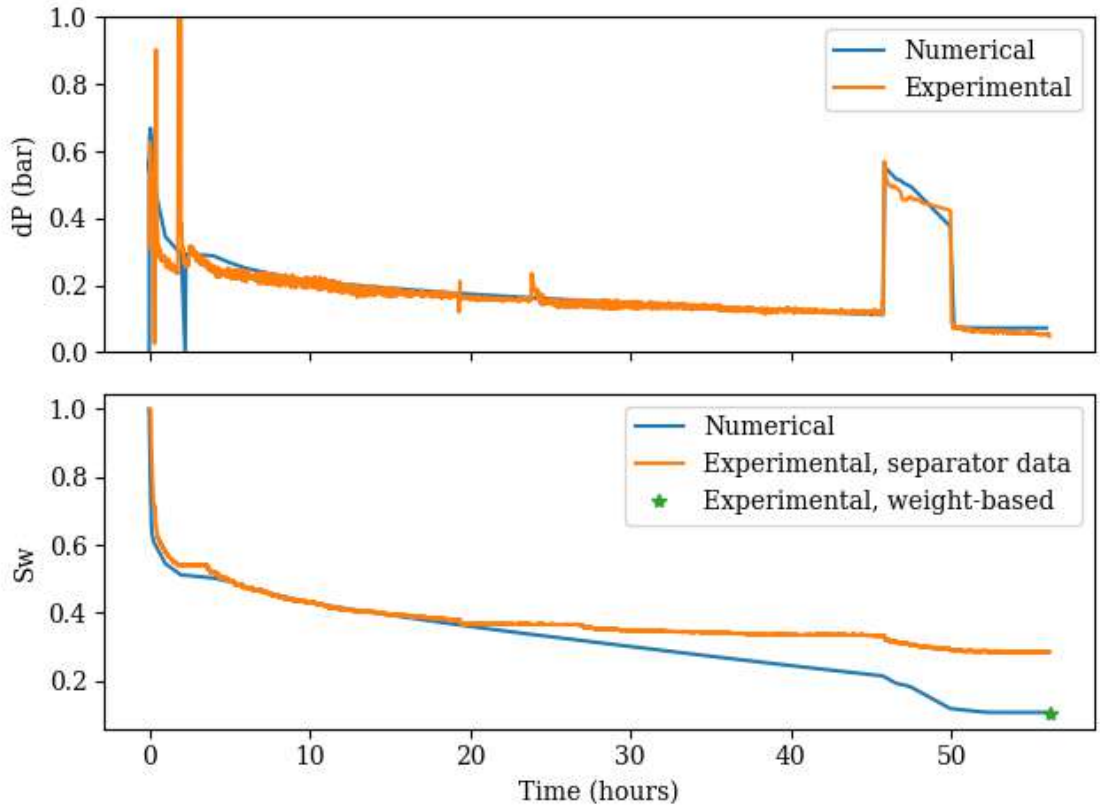

Figure 26. A comparison of the numerical and experimental results for the differential pressure (dP) and water saturations (Sw). The vertical axis for the dP plot are limited to the interval (0, 1) for better visibility of the results.

We argue that this behavior can be explained by an increased effect of water vaporization to the CO_2-rich phase. Indeed, the saturation values after 20 hours start to approach and to fall behind the critical water saturation S_{wc} (cf. Figure 25). Further decrease in S_w can only be due to water vaporization.

The experimental water saturation curve in Figure 26 is obtained by re-calculating production volumes in the separator without taking into account the phase transitions there, see Section 2.2. This is the reason for mismatch between the separator-based and weight-based estimate for water saturation at the end of the experiment (the orange curve and the green asterisk in Figure 25). Observe that the numerical results match perfectly the weight-measured experimental water saturation.

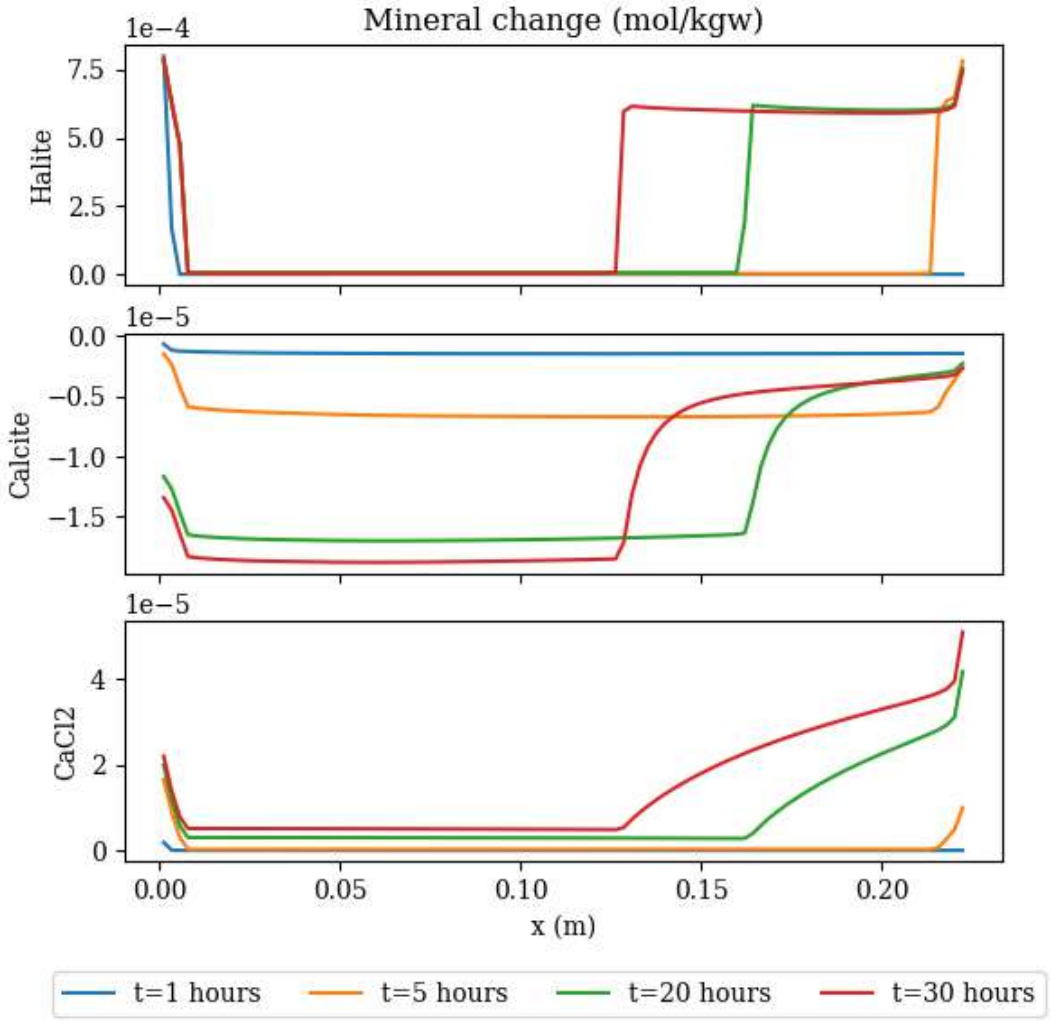

Figure 27. Numerical results for the precipitation (positive change) and dissolution (negative change) of the major minerals along the core for different time instants.

The numerical results for the major minerals are presented in Figure 27. For the first hour of CO_2 injection, halite and calcium chloride to precipitate while calcite dissolves close to the core inlet for small x. At approx. 2 hours, the flow direction is reverted, and the same effect is taking place at the opposite side of the core, see the results for 5, 20, and 30 hours. Note that the change in halite is considerably larger than the changes in calcite and in calcium chloride. These results are consistent with the petrophysical observations in Section 3.

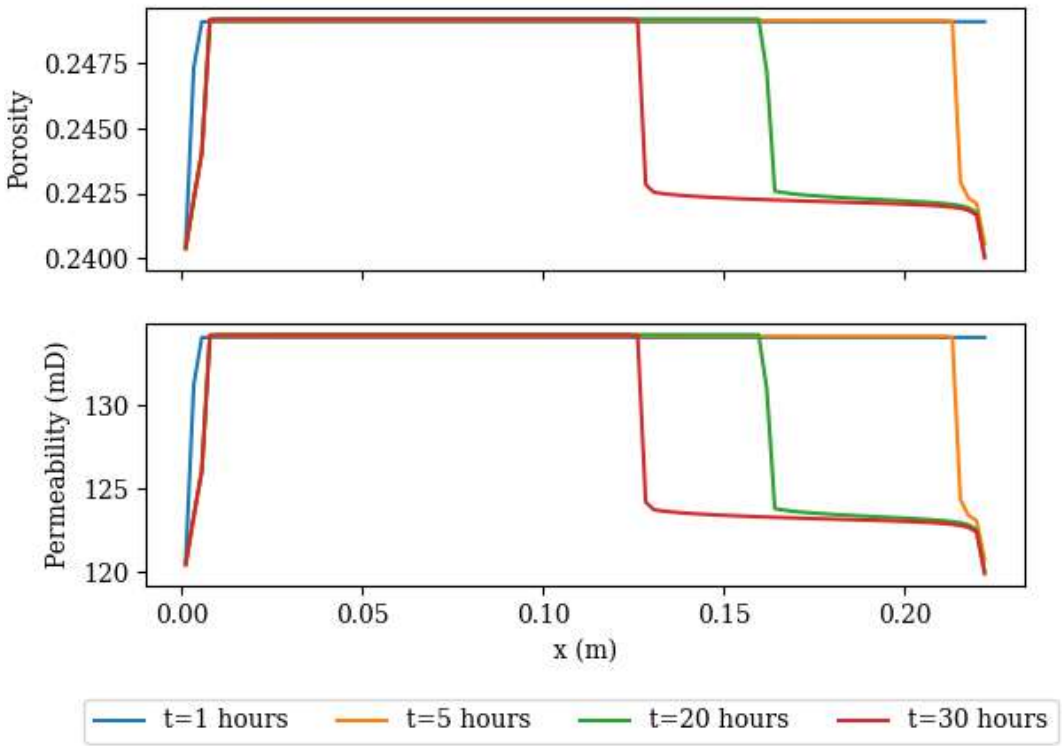

Figure 28. Numerical results for porosity and permeability alteration due to minerals' precipitation and dissolution.

The precipitated and dissolved minerals affect the sample porosity and permeability as illustrated in Figure 28. The porosity variation follows closely the halite precipitation dynamics. The permeability reduction, predicted by the Kozeny-Carman relationship, is of the order of 10%. This reduction is consistent with the experimental results of Section 2.2.

Conclusions

The present ConsenCUS deliverable D4.3 contains the results of core flooding experiments, petrophysical investigations, geochemical and fluid flow modelling aimed at constraining the uncertainties for CO_2 storage at the Stenlille site in Denmark. The experimental results indicate that there is a possibility of salt precipitation and fines migration due to CO_2 injection, but no indications of geomechanical failures have been observed. It should be stressed that the conducted experimental work was performed on a limited number of samples and additional studies are recommended for de-risking of CO_2 storage at Stenlille.

The conducted geochemical studies identify the reactions which will occur due to interaction of the injected CO_2 with impurities with the reservoir rock and fluid. A reactive fluid flow numerical model is presented which reproduces the measured experimental results with reasonable accuracy. The numerical results also agree well with qualitative characterization of geochemical reactions, available via petrographical investigations.

Fluid-rock interaction of CO_2 with reservoir rocks and with the formation brine is a complex phenomenon and several experimental and numerical challenges were encountered:

- The reason for sharp increase in differential pressure during core flooding is not clear; the available experimental data suggest several explanations for the observed behavior.
- There is a considerable variety of possible geochemical reactions which can occur in the considered fluid-rock system; more data (e.g., geochemical sampling and mCT scanning) is needed to better quantify the reaction parameters.
- Numerical simulation is a computationally intensive task even in the considered 1D case; depending on the choice of numerical parameters, the simulation time in some cases was up to an hour. Numerical simulation of full-scale reservoir models will require a considerable simplification of the model is order to be tractable.

The numerical fluid model, tuned to the experimental data in this work, will be subsequently used for modelling of realistic injection scenarios in the ConsenCUS deliverable 4.4.

Bibliography

American Petroleum Institute Data Book. (2005). *API databook.* Houston, Texas, USA: EPCON International.

Appelo, C. A., Parkhurst, D. L., & Post, V. E. (2014). Equations for calculating hydrogeochemical reactions of minerals and gases such as CO2 at high pressures and temperatures. *Geochim. Cosmochim. Acta, 125*, 49-67.

Bloomfield, J., & Williams, A. (1995). An empirical liquid permeability – gas permeability correlation for use in aquifer properties studies. *Quarterly Journal of Engineering Geology, 28*, 143-150.

Brooks, R., & Corey, A. (1964). *Hydraulic Properties of Porous Media.* Colorado State University: Fort Collins; Hydrology Papers.

Cadogan, S. P., Maitland, G. C., & Martin Trusler, J. P. (2014). Diffusion Coefficients of CO2 and N2 in Water at Temperatures between 298.15 K and 423.15 K at Pressures up to 45 MPa. *J. Chem. Eng. Data, 59*, 519−525.

Camy, S., Letourneau, J.-J., & Condoret, J.-S. (2011). Experimental study of high pressure phase equilibrium of (CO2 + NO2/N2O4) mixtures. *J. Chem. Thermodyn., 43*, 1954-1960.

CMG. (2022). *GEM Compositional & Unconventional Simulator*. Retrieved from https://www.cmgl.ca/gem.

Danckwerts, P. (1970). *Gas-liquid reactions.* New York: McGraw-Hill Book Co.

Helgeson, H. C. (1969). Thermodynamics of hydrothermal systems at elevated temperatures and pressures. *Am. J. Sci. , 267*, 729–804. doi:10.2475/ajs.267.7.729

Herning, F., & Zipperer, L. (1936). Gas Wasserfach. *Chemical Engineering Handbook, 1984*.

Ignarro, L., Fukuto, J., Griscavage, J., Rogers, N., & Byrns, R. (1993). Oxidation of nitric oxide in aqueous solution to nitrite but not nitrate: comparison with enzymatically formed nitric oxide from L-arginine. *Proc. Natl. Acad. Sci., 90*, 8103–8107.

Jossi, J., Stiel, L., & Thodos, G. (1962). The Viscosity of Pure Substances in the Dense Gaseous and Liquid Phases. *AIChE Journal, 8*, 59-63.

Kestin, J., Khalifa, H., & Correia, R. (1981). Tables of the Dynamic and Kinematic Viscosity of Aqueous NaCl Solutions in the Temperature Range 20-150 °C and Pressure Range 0.1-35 MPa. *J. Phys. Chem. Ref. Data, 10*, 71-87.

Kestin, J., Khalifa, H., Abe, Y., Grimes, C., Sookiazian, H., & Wakeham, W. (1978). The effect of pressure on the viscosity of aqueous NaCl solutions in the temperature range 20-150 °C. *J. Chem. Eng. Data, 23*(4), 328-336.

Larson, T., Horike, N., & Harrison, H. (1977). Oxidation of sulfur dioxide by oxygen and ozone in aqueous solution: a kinetic study with significance to atmospheric processes. *Atmos. Environ., 12*, 1597–1611.

Lee, Y., & Schwartz, S. (1981). Reaction kinetics of nitrogen dioxide with liquid water at low partial pressure. *J. Phys. Chem., 85*, 840–848.

Lewis, R., & Deen, W. (1994). Kinetics of the reaction of nitric oxide with oxygen in aqueous solutions. *Chem. Res. Toxicol., 7*, 568–574.

Littlejohn, D., Hu, K., & Chang, S. (1986). Kinetics of the reaction of nitric oxide with sulfite and bisulfite ions in aqueous solution. *Inorg. Chem., 25*, 3131–3135.

Luna-Ortiz, E., Yao, C., Barnes, J., Winter, M., & Healey, M. (2022). Development of A CO2 Specification for Industrial CCS Transport Networks: Methodology, Limitations and Opportunities. *Offshore Technology Conference.* doi:10.4043/32103-MS

Martin, L., Damschen, D., & Judeikis, H. (1980). The reactions of nitrogen oxides with SO2 in aqueous aerosols. *Atmos. Environ., 15*, 191–195.

Millero, F. J., Sotolongo, S., & Izaguirre, M. (1987). The oxidation kinetics of Fe(II) in seawater. *Geochim. Cosmochim. Acta, 51*, 793–801.

Möller, D. (1988). Kinetic model of atmospheric SO2 oxidation based on published data. *Atmos. Environ. (1967), 14*, 1067-1076.

Morgan, B., Lahav, & O. (2007). The effect of pH on the kinetics of spontaneous Fe(II) oxidation by O2 in aqueous solution – basic principles and a simple heuristic description. *Chemosphere, 68*, 2080–2084.

NIST Chemistry Webbook: National Institute of Standards and Technology. (2023). Retrieved from https://webbook.nist.gov/chemistry/

Oblath, S., Markowitz, S., Novakov, T., & Chang, S. (1982). Kinetics of the initial reaction of nitrite ion in bisulfite solutions. *J. Phys. Chem., 86*, 4853–4857.

Park, J., & Lee, Y. (1988). Solubility and decomposition kinetics of nitrous acid in aqueous solution. *J. Phys. Chem., 92*, 6294–6302.

Parkhurst, D. L., & Appelo, C. A. (2013). *Description of input and examples for PHREEQC. Version 3 – A computer program for speciation, batch-reaction, one-dimensional transport, and inverse geochemical calculations.* U.S. Geological Survey.

Peng, D.-Y., & Robinson, D. B. (1976). A New Two-Constant Equation of State. *Ind. Eng. Chem. Fundamen., 15*, 59-64.

Plummer, L., Parkhurst, D., Fleming, G., & Dunkle, S. (1988). *A computer program incorporating Pitzer's equations for calculation of geochemical reactions in brines.* U.S. Geological Survey.

Pruess, K. (2005). *ECO2N: A TOUGH2 Fluid Property Module for Mixtures of Water, NaCl, and CO2.* University of California, Lawrence Berkeley National Laboratory.

Rumpf, B., & Maurer, G. (1992). Solubilities of hydrogen cyanide and sulfur dioxide in water at temperatures from 293.15 to 413.15 K and pressures up to 2.5 MPa. *Fluid Phase Equilib., 81*, 241-260.

Rütters, H., Fischer, S., Hoa, L., Bettge, D., Bäßler, R., & Maßmann, J. (2022). Towards defining reasonable minimum composition thresholds – Impacts ofvariable CO2 stream compositions on transport, injection and storage. *Int. J. Greenh. Gas Control* , 103589.

Sander, R. (1999). Modeling atmospheric chemistry: Interactions between gas-phase species and liquid cloud/aerosol particles. *Surv. Geophys., 20*, 1–31.

Shock, E., Helgeson, H., & Sverjensky, D. (1989). Calculation of the thermodynamic and transport properties of aqueous species at high pressures and temperatures: Standard partial molal properties of inorganic neutral species. *Geochim. Cosmochim. Acta, 53*, 2157-2183.

Sonnenthal, E., Xu, T., Spycher, N., & Zheng, L. (2021). TOUGHREACT V4.13-OMP & TReactMech V1.0: Geochemical and Reactive-Transport User Guide.

Spycher, N. F., Llanos, E. M., & Haese, R. R. (2019). Reservoir scale reactive-transport modeling of a buoyancy-controlled CO2 plume with impurities (SO2, NO2, O2). *Int. J. Greenh. Gas Control, 89*, 40–51.

Spycher, N., Zhang, G., Sonnenthal, E., & Molis, S. (2021). *TOUGHREACT-Brine: Supplement to TOUGHREACT-V4.0-OMP User's Guide for Modeling Concentrated Solutions and Osmosis Using the Pitzer Ion-Interaction Model.* Lawrence Berkeley National Laboratory.

Squadrito, G. L., & Postlethwait, E. M. (2009). On the hydrophobicity of nitrogen dioxide: Could there be a "lens" effect for NO2 reaction kinetics? *Nitric Oxide, 21*, 104-109.

Sterpenich, J., Caumon, M.-C., Lachet, V., Creton, B., El Jarmouni, M., Randi, A., & Robert, P. (2022). NO solubility in water and brine up to 60 MPa and 373 K by combining Raman spectroscopy and molecular simulation. *J. Raman Spectrosc., 53*, 645-653.

Talman, S. (2015). Subsurface geochemical fate and effects of impurities contained in a CO2 stream injected into a deep saline aquifer: what is known. *Int. J. Greenh. Gas Control, 40*, 267–291.

Tosun, I. (2021). Appendix A - Critical constants and acentric factors. In *The Thermodynamics of Phase and Reaction Equilibria* (pp. 749-751). Elsevier.

Wang, J., Li, J., Ye, J., Zhao, J., Wu, Y., & Hu, J. (2020). Fast sulfate formation from oxidation of SO2 by NO2 and HONO observed in Beijing haze. *Nat. Commun.*, 1–7.

Weibel, R., Kjøller, C., Bateman, K., Laier, T., Nielsen, L. H., & Purser, G. (2014). Carbonate dissolution in Mesozoic sandstones as a response to CO2 exposure at 70°C and 20 MPa. *Applied Geochemistry, 42*, 1-15.

Weibel, R., Olivarius, M., Kristensen, L., Friis, H., Hjuler, M. L., . . . Nielsen, L. H. (2017). Predicting permeability of low enthalpy geothermal reservoirs: A case study from the

Upper Triassic−Lower Jurassic Gassum Formation, Norwegian–Danish Basin. *Geothermics, 65*, 135-157.

Xu, T., Spycher, N., Sonnenthal, E., Zhang, G., Zheng, L., & Pruess, K. (2011). TOUGHREACT Version 2.0: a simulator for subsurface reactive transport under non-isothermal multiphase flow conditions. *Computers & Geosciences, 37*, 763-774.

Yoon, P., & Thodos, G. (1970). Viscosity of Nonpolar Gaseous Mixtures at Normal Pressures. *AIChE Journal, 16*, 300-304.